Volume 4
Number 1
January 2025
Pages 1–182

Environmental Science Advances

rsc.li/esadvances

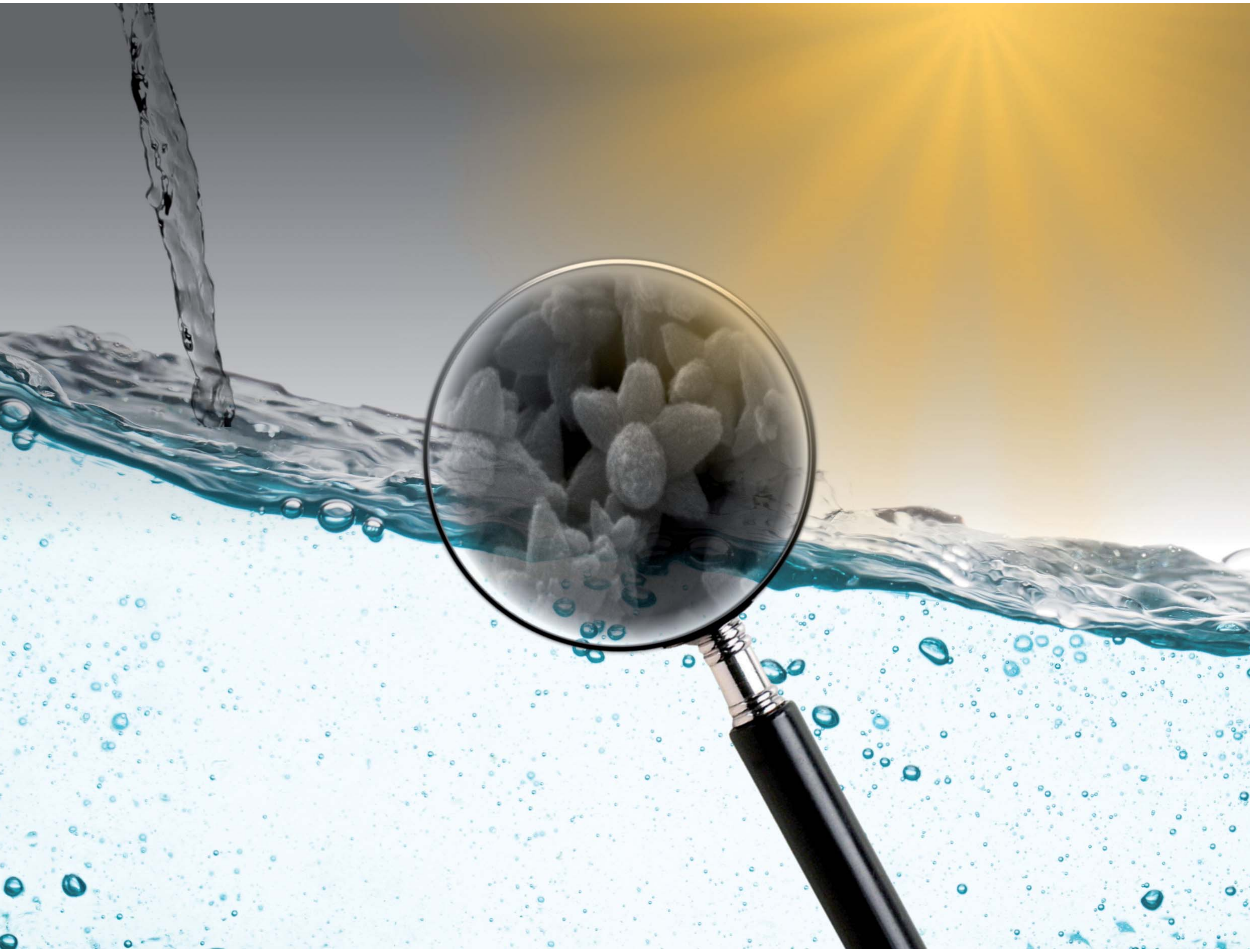

ISSN 2754-7000

ROYAL SOCIETY OF **CHEMISTRY**

PAPER
Sougata Ghosh *et al.*
Green synthesis of silver and copper-doped zinc oxide nanoflowers using *Leucophyllum frutescens* leaf extract for photodegradation of methylene blue dye and antibacterial applications

Environmental Science
Advances

ROYAL SOCIETY
OF CHEMISTRY

PAPER

View Article Online
View Journal | View Issue

Check for updates

Cite this: *Environ. Sci.: Adv.*, 2025, **4**, 97

Green synthesis of silver and copper-doped zinc oxide nanoflowers using *Leucophyllum frutescens* leaf extract for photodegradation of methylene blue dye and antibacterial applications†

Maitri Nandasana,[a] Tanawat Imboon,[b] Rashbihari Layek,[c] Arindam Dey,[c] Pranav Pandya,[a] Vijay Singh Parihar,[d] Madhumita S. Tawre,[e] Santosh Sutar,[f] Pathik Kumbhakar,[c] Karishma Pardesi,[e] Sirikanjana Thongmee[b] and Sougata Ghosh *[ab]

Received 28th July 2024
Accepted 2nd October 2024

DOI: 10.1039/d4va00295d

rsc.li/esadvances

The present work unveils a process to synthesize silver (Ag) and copper (Cu) doped zinc oxide (ZnO) nanoflowers for photocatalytic and antibacterial applications. *Leucophyllum frutescens* leaf extract (LFLE) was used for the rapid and efficient green synthesis of nanoparticles (NPs). The current study provides new insight into the fabrication of uniform exotic NPs with tunable size and shape that control their photocatalytic and therapeutic potential. UV-visible and photoluminescent spectroscopy exhibited the optical properties. The energy bandgap of 3.36 eV in the ZnONPs was reduced to 3.26, 3.21, and 3.24 eV, in Ag@ZnONPs, Cu@ZnONPs, and Ag–Cu@ZnONPs, respectively as calculated from the Tauc plots. Field-emission scanning electron microscope and high-resolution transmission electron microscope images revealed the flower-shaped morphology of the NPs. At the same time, energy dispersive spectra and elemental mapping confirmed the presence of Zn, O, Ag, and Cu in the respective NPs. X-ray diffraction confirmed the crystalline nature with the average crystallite size being 12.75 nm, 11.22 nm, 13.14 nm, and 13.23 nm for ZnONPs, Ag@ZnONPs, Cu@ZnONPs, and Ag–Cu@ZnONPs. Photocatalytic degradation of methylene blue dye was maximum in the Ag–Cu@ZnONPs that closely fitted with the pseudo-first-order reaction kinetics. Additionally, the Ag@ZnONPs with a higher aspect ratio due to smaller size resulted in superior antibacterial activity and synergy with antibiotics against *Bacillus subtilis*, *Staphylococcus aureus*, and *Pseudomonas aeruginosa*. The results confirm the nanobiotechnological potential of *L. frutescens* which can be used for environmental remediation.

Environmental significance

Recent advances in the area of nanotechnology have helped to develop affordable, eco-friendly, and sustainable processes for fabrication of nanomaterials for environmental applications. The functionality of nanomaterials depends on their structural properties. Hence, reducing agents and stabilizing agents are added to have control over the shape and size of the nanoparticles. However, these chemicals are often hazardous and pose significant risk to the environment. More recently, biogenic synthesis has emerged as a complementary and alternative strategy which is rapid, efficient, and environmentally benign. However, the major challenge is relatively high polydispersity and lack of control over the dimensions. In the current study, we aim to circumvent such issues by fabricating flower like undoped and silver/copper doped zinc oxide nanoparticles using *Leucophyllum frutescens* leaf extract. Furthermore, the nanoflowers exhibited photocatalytic degradation of dyes and antibacterial synergy in combination with antibiotics. Thus, this work emphasizes that phytogenic nanoflowers are promising agents for preventing dye pollution and bacterial infection with no negative implications on the environment.

---

[a] *Department of Microbiology, School of Science, RK University, Rajkot-260020, Gujarat, India. E-mail: ghoshsibb@gmail.com; Tel: +91-9909952030, ext. 303*

[b] *Department of Physics, Faculty of Science, Kasetsart University, Bangkok-10900, Thailand*

[c] *Department of Physics, National Institute of Technology Durgapur, Durgapur-713209, West Bengal, India*

[d] *Biomaterials and Tissue Engineering Group, Faculty of Medicine and Health Technology, Tampere University, Tampere-33720, Finland*

[e] *Department of Microbiology, Savitribai Phule Pune University, Pune-411007, Maharashtra, India*

[f] *Yashwantrao Chavan School of Rural Development, Shivaji University, Kolhapur-416004, Maharashtra, India*

† Electronic supplementary information (ESI) available. See DOI: https://doi.org/10.1039/d4va00295d

1. Introduction

Nanomaterials with a large surface area to volume ratio exhibit superior thermal conductivity, catalytic activity, and non-linear optical properties. They have immense applications in food, agriculture, pharmaceuticals, cosmetics, and healthcare.[1,2] It is important to note that the activity of the nanoparticles (NPs) is defined by their shape and size. Hence, several processes like chemical co-precipitation, vapor deposition, hydrothermal, microwave-assisted combustion, pulsed laser deposition, sol–gel process, solvothermal, and spray pyrolysis methods are employed for the synthesis of the NPs.[3]

Among various types of inorganic metal oxides, zinc oxide nanoparticles (ZnONPs) are considered GRAS (generally recognized as safe). Their large band gap (3.37 eV) and high exciton binding energy (60 meV) are attributed to notable semiconducting properties. Apart from their catalytic and optical properties, they have significant therapeutic potential because of their antioxidant, antidiabetic, antimicrobial, and anticancer activities. They have piezoelectric and pyroelectric properties and are used in industries associated with rubber and paint. ZnONPs can vary in their morphology including nanobelts, nanocages, nanocombs, nanoflakes, nanoflowers, nanoneedles, nanorings, nanorods, nanospheres, nanosprings, nanotubes, and nanowires.[4]

There is a gap in the development of new strategies to alter the catalytic, electrical, magnetic, mechanical, morphological, optical, and photochemical properties of ZnONPs by rational doping with appropriate elements.[5] The photoresponse of ZnONPs can be enhanced by silver (Ag) doping where the diminution of the donor defect concentration compensates for the n-type conductivity. The quasi-one-dimensional (Q1-D) ZnO:Ag forms the building blocks of large multifunctional nanomaterials with attractive geometry and physicochemical properties.[6] Doping of Ag, an electron acceptor, in ZnONPs allegedly influences the optical properties resulting in enhanced luminescence and p-type conductivity.[7] The higher photocatalytic potential of the Ag-doped ZnONPs is attributed to the separation of charges and increase in the photo-generated charges. This can be exploited for the removal of refractory pollutants from industrial effluents.[8]

It is advantageous to use another important dopant, copper (Cu) which has an almost identical ionic radius to ZnO.[9,10] New energy levels can be created within the bandgap as defects are generated in the lattice of ZnONPs during doping. Furthermore, the lattice dynamics associated properties are altered as the active mass and force in the native lattice vary.[11]

Recently, the fabrication of multi-metal doped hybrid nanomaterials has received much attention as this strategy generated new and improved functionality apart from just altering the properties of individual NPs. However, multi-metal doped ZnONPs are synthesized mostly by ball milling, co-precipitation, sol–gel, and hydrothermal/solvothermal processes where the chemicals used as reducing and capping agents are often hazardous and toxic.[12–14] Thus, it is significant to develop an environmentally benign green route for synthesis of metal-doped ZnONPs. Among various types of biofabrication processes, medicinal plant-mediated synthesis of NPs is the most attractive as it is nontoxic.

The nanobiotechnological aspects of the drought-tolerant shrub, *Leucophyllum frutescens* are mostly unexplored to date. The plant is used in traditional medicine for treating asthma, bladder disorders, cancer, cough, fever, and tuberculosis. It can serve as an analgesic, antioxidant, and vasodilator.[15] It has a plethora of bioactive compounds such as anthocyanin, asarinin, carotenoids, epigallocatechin, eridictoyl, eudesmin, leubethanol, lutein, lycopene, myricetin-3-acetylrhamnoside, pinoresinol diglucoside, propyl gallate, quercetin-3-*O*-glucoside, and theobromine that can play a vital role in the synthesis of NPs and stabilization. Hence, it would be interesting to develop green synthesis of multi-metal doped ZnONPs using *L. frutescens*.[16–18]

One of the most important applications of nanotechnology is the photocatalytic degradation of artificial dyes widely used in the textile, leather, pharmaceutical, food and cosmetic industries. Release of the untreated residual dyes in the waterbodies causes a significant threat to health and the environment.[19,20] Thus, heterogeneous photocatalysis is employed for degrading the toxic dyes under illumination of the semiconductor surface with light of an appropriate wavelength. The generated electron–hole pairs and subsequent transfer of the electrons from the valence band (VB) to the conduction band (CB) are associated with the generation of free radicals that can effectively degrade the treated dye.[21]

This is the first study to report the synthesis of Ag–Cu-codoped ZnO nanoflowers using *L. frutescens* leaf extract and test their photocatalytic dye degrading ability. The hybrid NPs were characterized and their properties were compared with those of the mono-metal doped and undoped ZnO nanoflowers.

2. Materials and methods

2.1 Chemicals and reagents

Zinc nitrate hexahydrate ($Zn(NO_3)_2\cdot6H_2O$), silver nitrate ($AgNO_3$), potassium bromide (KBr), and ethylenediaminetetraacetic acid disodium salt dihydrate ($C_{10}H_{14}N_2O_8Na_2\cdot2H_2O$) were purchased from Sisco Research Laboratories (SRL) Pvt. Ltd, India. Copper(II) nitrate ($Cu(NO_3)_2\cdot3H_2O$), sodium hydroxide pellets (NaOH), and potassium dichromate ($K_2Cr_2O_7$) were procured from Oxford Laboratory, HiMedia Laboratories Pvt. Ltd, and Molychem, India, respectively. Ethyl alcohol (C_2H_5OH) and methylene blue dye were purchased from Shree Chalthan Vibhag Khand Udyog Sahakari Ltd, India and Merck Specialties, Germany, respectively. All chemicals used were of analytical reagent (AR) grade.

2.2 Plant extract preparation

L. frutescens samples were collected from RK University campus, Rajkot, India (22.2404° N, 70.9004° E). The twig composed of leaves, flowers, and buds was used for herbarium preparation that was authenticated by the Department of Biosciences, Saurashtra University, India. The fresh leaves were washed

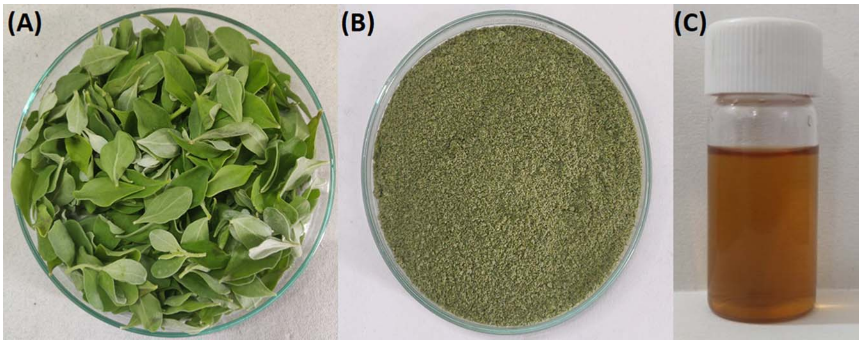

Fig. 1 LFLE preparation. (A) Fresh leaves of *L. frutescens*; (B) pulverized dry leaves; (C) LFLE.

thoroughly with distilled water followed by shade drying as shown in Fig. 1. The dried leaves were pulverized to a fine powder in an electric blender. The *L. frutescens* leaf extract (LFLE) was prepared by adding 5 g of the resulting leaf powder to 100 mL of distilled water in a conical flask (250 mL) that was boiled at 100 °C in a water bath for 5 min. The extract was centrifuged at 5000 rpm for 30 min to remove the plant biomass and the supernatant was filtered using Whatman filter paper no 1. The resulting LFLE was stored at 4 °C for further experiments.[22]

2.3 Synthesis of NPs

The undoped and doped ZnONPs were synthesized following the procedures adopted by combining the previous reports with necessary modifications.[23,24] For, ZnONP synthesis, the LFLE (1 mL) was added to 50 mL (0.01 M) zinc nitrate hexahydrate ($Zn(NO_3)_2 \cdot 6H_2O$) while the fabrication of silver doped ZnONPs (Ag@ZnONPs) was carried out by addition of 0.01 M of $Zn(NO_3)_2 \cdot 6H_2O$ and 5% of silver nitrate ($AgNO_3$) into 50 mL water followed by the addition of 1 mL LFLE.[25] In the case of copper-doped ZnONPs (Cu@ZnONPs), 0.01 M of $Zn(NO_3)_2 \cdot 6H_2O$ was mixed with 5% of copper(II) nitrate trihydrate ($Cu(NO_3)_2 \cdot 3H_2O$) in 50 mL water followed by the addition of 1 mL LFLE.[26] Silver and copper-doped ZnONPs (Ag–Cu@ZnONPs) were synthesized by reacting 0.01 M of $Zn(NO_3)_2 \cdot 6H_2O$ with 5% each of $AgNO_3$ and $Cu(NO_3)_2 \cdot 3H_2O$ in 50 mL water followed by the addition of 1 mL LFLE.[27] All reaction mixtures were stirred at 60 °C for 24 h and the pH was adjusted to 12 using 5 M NaOH. The precipitates were recovered by centrifugation at 15 000 rpm for 10 min, after which the supernatant was discarded. The resulting pellets were re-suspended in 1.5 mL of distilled water and centrifuged again under the aforementioned conditions. This washing step was repeated twice. The pellets were then suspended in 1 mL of ethyl alcohol and centrifuged at 15 000 rpm for 10 min. The recovered pellets were suspended in 1 mL of water and transferred to a crucible and dried overnight at room temperature followed by calcination at 400 °C for 2 h.

2.4 Characterization

The UV-visible absorption spectra of the biosynthesized ZnONPs, Ag@ZnONPs, Cu@ZnONPs, and Ag–Cu@ZnONPs were recorded using a Shimadzu UV-1900 UV-vis spectrophotometer. Washed and dried NPs (10 mg) were suspended in 50 mL of distilled water and sonicated for 30 min. The suspension was transferred to a quartz cuvette and UV-vis spectra were recorded with a wavelength range of 200–800 nm. The measurement speed was set to "slow" with an interval of 0.5. The absorption graphs were plotted for absorbance (a.u.) *vs.* wavelength (nm). The synthesis of the nanoparticles was carried out for 24 h which led to a visible change in the color of the reaction mixture as shown in the insets of Fig. 2. During ZnONP synthesis, the color of the solution changed from yellow to white where precipitation was noted at the bottom. The fabrication of Ag@ZnONPs was marked with an appearance of brown color while white color appeared for Cu@ZnONPs after 24 h. In the case of Ag–Cu@ZnONPs, a yellowish-brown color was developed in the reaction mixture after the completion of the synthesis. The photoluminescence (PL) spectra of the NPs were obtained using a PerkinElmer LS-55 spectrofluorometer within the wavelength range of 200–800 nm, under different excitation wavelengths (λ_{ex}). The NPs were dispersed separately in DI water at identical concentrations (1 mg mL^{-1}) and taken in a 4-side transparent, 1 cm × 1 cm quartz cuvette for recording the PL spectra.[28] The size and shape of the NPs were evaluated using a field emission scanning electron microscope (FEI Quanta 450) working at an accelerating voltage of ~30 kV followed by elemental mapping. Elemental composition was confirmed using an energy-dispersive X-ray spectroscope (Oxford Instruments X-max 50 mm^2). A field emission transmission electron microscope (JEOL JEM 3100F) operated at 300 kV was employed to record the high-resolution images of the NPs that were loaded on carbon-coated copper grids. Particle size analysis was conducted and zeta potential was measured using a NanoBrook Omni (Brookhaven Instruments). The crystallinity of the NPs was examined by XRD pattern analysis (AXS D8 Focus P-XRD, Bruker), at a voltage of 40.0 kV and a current of 40.0 mA. The FTIR spectra of the undoped and doped ZnONPs were recorded in the range of 500–3500 cm^{-1} using an IRSpirit FTIR spectrophotometer, Shimadzu. After completion of the synthesis, the reaction mixture was centrifuged at 10 000 rpm for 15 min at room temperature. The supernatant containing the LFLE was collected and was dried and analyzed by FTIR using the KBr pellet method and compared with the LFLE before synthesis.

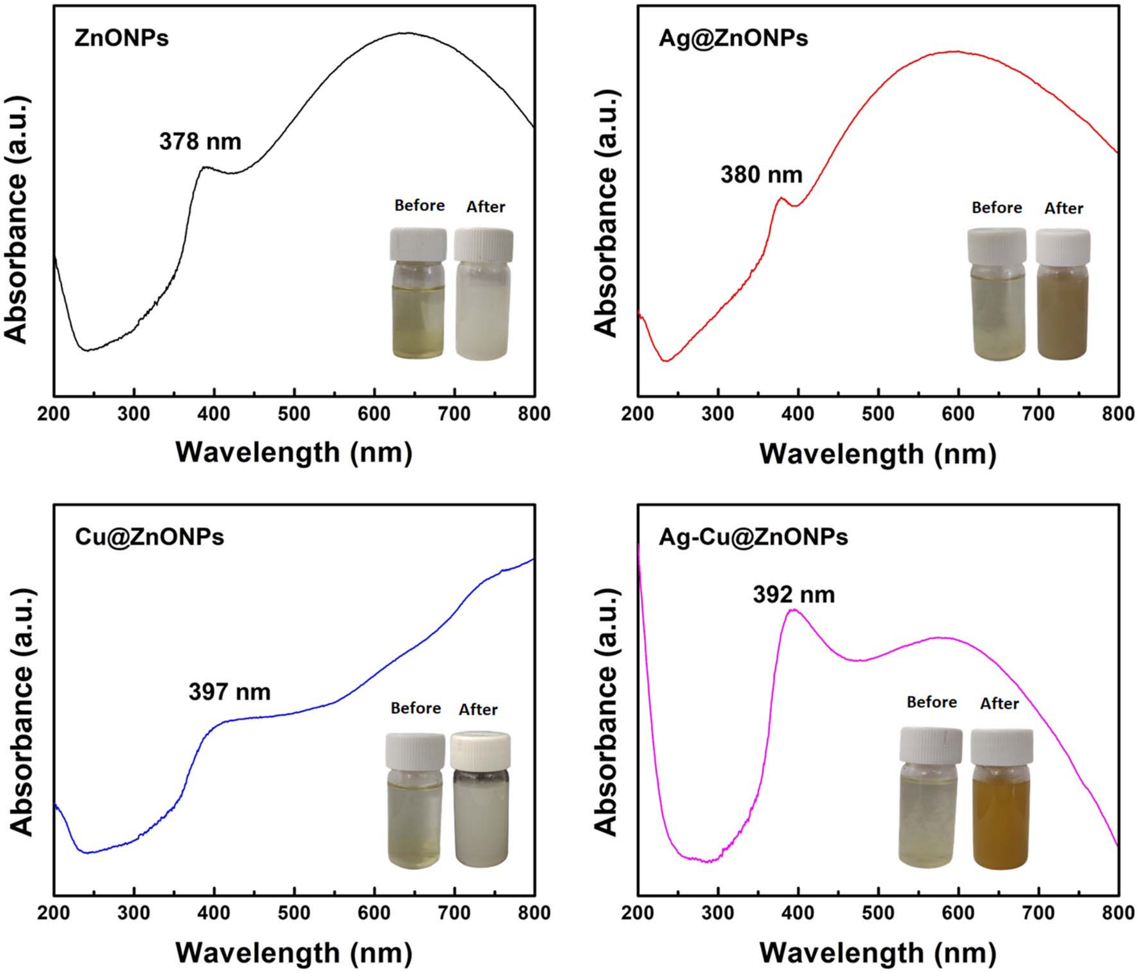

Fig. 2 UV-visible spectra of the undoped and doped ZnONPs; the insets present the color change before and after synthesis.

2.5 Photocatalytic dye degradation

The biogenic ZnONPs, Ag@ZnONPs, Cu@ZnONPs and Ag–Cu@ZnONPs were checked for catalytic activity using methylene blue (MB) dye. The initial MB dye concentration was 20 mg L^{-1}. The photocatalytic dye degradation efficiency of the biogenic NPs was examined by degrading the MB dye under a visible light of intensity 30k LUX. In this measurement, 20 mg per L MB was dissolved in 50 mL of DI water. Then, 0.4 g L^{-1} of each catalyst (NPs) was added to the solution separately. After that, the mixed solution was stirred in a dark environment for 1 h to achieve the adsorption/desorption equilibrium conditions. An amount of 3 mL of the aliquot was collected and centrifuged after each 10 min interval, and then the supernatant was used to measure the intensity of MB dye at 662 nm. The rate of dye degradation was calculated using the following formula: photocatalytic dye degradation (%) = $(C_0 - C_t)/C_0 \times 100\%$, where C_0 represents the initial dye concentration and C_t represents the final dye concentration after treatment for a specific time interval (t). Additionally, the effect of pH, concentrations of NPs and MB was evaluated. The role of a free radical scavenger, EDTA-2Na, at a concentration of 1 mM was studied in the dye degradation process in the presence of the NPs.

2.6 Antibacterial synergy

The inhibitory effect of the NPs was tested against both Gram-positive (*Bacillus subtilis* MTCC 441 and *Staphylococcus aureus* subsp. *aureus* MTCC 737) and Gram-negative (*Pseudomonas aeruginosa* MTCC 424) bacteria using the agar well diffusion method on Mueller–Hinton agar (MHA) plates. Each bacterial strain was inoculated into the Mueller–Hinton broth (MHB) individually and incubated overnight at 180 rpm and 37 °C. The bacterial cultures (100 μL, $O.D_{600} = 0.1$) were spread on the MHA plates, and wells were prepared using a cork-borer (5 mm). The NPs (100 μg) were added into each well, and streptomycin and water were used as the positive and negative control, respectively. The plant extract was also checked for possible antibacterial activity. The plates were incubated at 37 °C for 24 h and the zone of inhibition (ZOI) was measured.[29]

The antimicrobial synergy was checked for the NPs with different antibiotics like streptomycin (ST), ampicillin (AM), and novobiocin (NB) where each well contained 100 μg of NPs and 50 μg of antibiotics together. Individual antibiotics and water were used as positive and negative controls, respectively. The plates were incubated under the same conditions mentioned before and an increase in the ZOI was checked. The synergy was expressed as a fold increase in the ZOI for the NP–antibiotic combination compared to only antibiotics.[30]

2.7 Statistical analysis

Statistical significance was determined by two factor analysis of variance (ANOVA). A statistically significant result was defined as one with a p-value of less than 0.05 ($*p < 0.05$).

3. Results and discussion

3.1 UV-vis spectral analyses

The UV-vis spectral analysis confirmed the successful fabrication of ZnONPs, Ag@ZnONPs, Cu@ZnONPs, and Ag–Cu@ZnONPs. The UV-vis absorption spectra of the synthesized ZnONPs in Fig. 2 showed a broad absorption in the range of 200–800 nm. A strong absorption peak of ZnONPs was observed at 378 nm. The characteristic peak of ZnONPs in the absorption spectra is attributed to the intrinsic band gap adsorption of ZnONPs that is associated with the transitions of electrons from the valence band to the conduction band. This observation is well in agreement with a previous report where ZnONPs were synthesized using *Mussaenda frondosa* and leaves of *Ziziphus nummularia*.[31,32] A similar intense peak at 390 nm was also noted during the synthesis of ZnONPs using *Papaver somniferum* L.[33] Ag@ZnONPs exhibited the peaks of ZnONPs at 380 nm. The doping of Ag on the ZnONPs resulted in the red shifting of the absorption peak which was similar to the findings observed by Islam *et al.* (2023) after the doping of ZnONPs with Ag using the sol–gel method.[34] This red shift in the excitonic peak was due to the coupling interaction resulting in the transfer of electrons between Ag and Zn as reported by Ghosh *et al.* (2012).[30]

In the case of Cu@ZnONPs, the peak at 397 nm was associated with the ZnONPs. The absorption spectra of Cu@ZnONPs showing a red shifting of characteristic peaks comply with the previous findings of Khan *et al.* (2020) as they fabricated Cu@ZnONPs using the leaf extract of *Stachytarpheta jamaicensis*.[35] The addition of Cu in ZnONPs resulted in the shifting of the absorption peak to a higher wavelength which resulted from the impurity band formation in the band gap of ZnO.[36]

The absorption spectra of Ag–Cu@ZnONPs demonstrated the characteristic peak for ZnONPs at 392 nm that was attributed to Ag and Cu dual doping in ZnONPs. This red shifting of the absorption peak due to the surface plasmon resonance

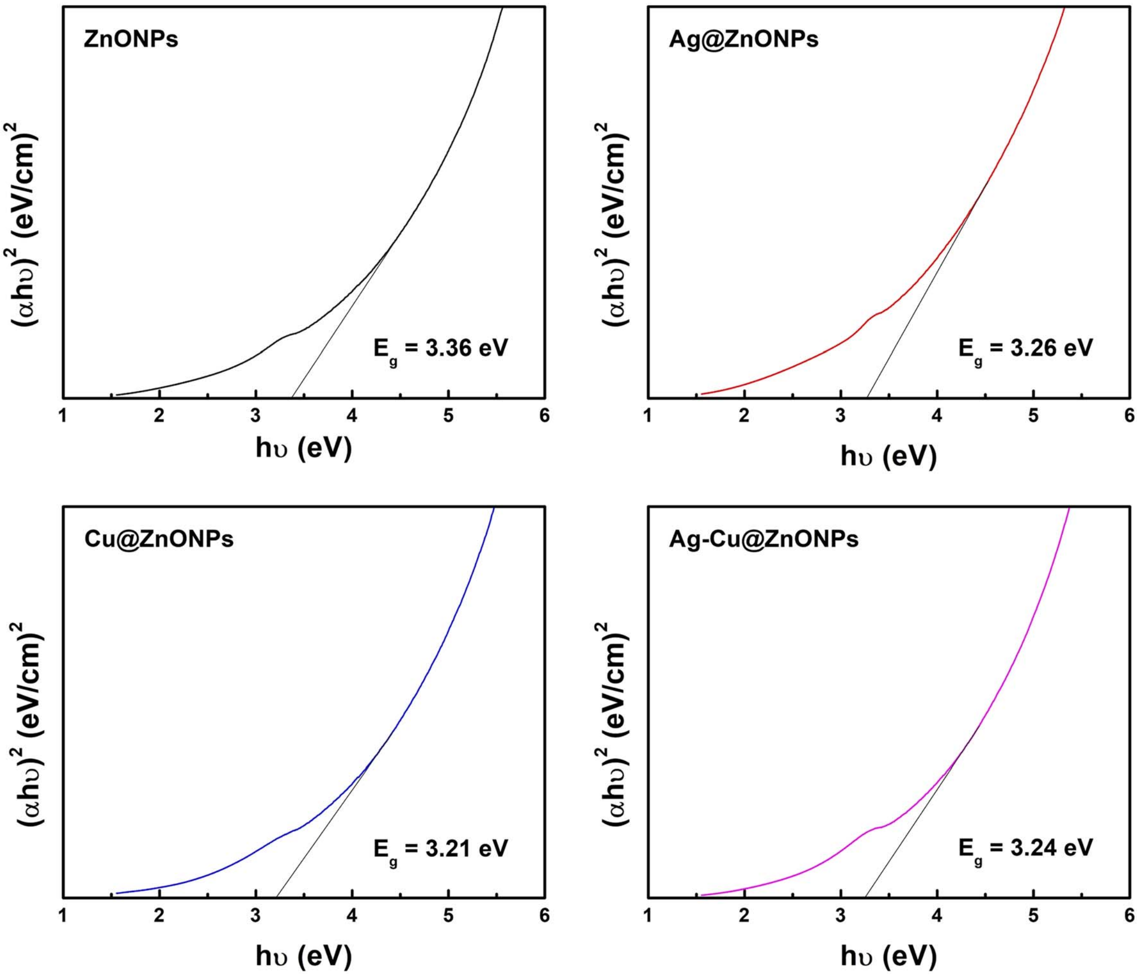

Fig. 3 Tauc plot of undoped and doped ZnONPs to determine the optical band gap.

(SPR) properties of Ag and Cu is similar to the previous findings on Ag–Cu@ZnO nanocomposite synthesized from the bark extract of *Aglaia roxburghiana*.[37]

The band gap energy was measured using a UV-vis spectrophotometer to characterize the optical properties. The band gap value can be calculated using the fundamental absorption, which corresponds to electron excitation from the valence band to the conduction band, by using Tauc's formula, given by the equation:

$$(\alpha h\nu)^n = K(h\nu - E_g)$$

where $h\nu$ is the photon energy, α is the absorption coefficient, K is a constant, E_g is the band gap energy, and the value of n is 2 for the direct band gap and 1/2 for the indirect band gap. The variation of $(\alpha h\nu)^2$ *vs.* $h\nu$ in Fig. 3 shows that the extrapolation of the linear portion to the x-axis gives the energy gap of the samples. The band gap energy values of ZnONPs, Ag@ZnONPs, Cu@ZnONPs, and Ag–Cu@ZnONPs were calculated by using a direct band gap, as ZnO is a direct band gap semiconductor. The energy gap values for ZnONPs, Ag@ZnONPs, Cu@ZnONPs, and Ag–Cu@ZnONPs were 3.36, 3.26, 3.21, and 3.24 eV, respectively. The decrease in band gap energies for the doped ZnONPs indicates changes in the nanocrystal electronic structure of the doped ZnO, resulting in more efficient light absorption.

3.2 PL spectral analyses

Fig. 4 depicts the PL emission spectra for all NPs at $\lambda_{ex} = 300$ nm. For all of the NPs, the PL spectra exhibited multiple peak emission nature. As shown in the figure, the PL emission peaks for ZnONPs are situated at 336 nm, 423 nm, 446 nm, 487 nm, 535 nm, and 653 nm respectively, with a central peak at 423 nm having the highest intensity. Arya *et al.* (2017) also reported a similar peak at 415 nm that was associated with the near band-edge emission (NBE), while the broad green emission was attributed to the recombination of holes with electrons that were trapped within the singly ionized oxygen vacancies.[38] In another study, the PL spectra of ZnONPs synthesized using *Phoenix dactylifera* showed similar peaks (446, 467, and 484 nm) in the blue zone which were speculated to be associated with the structural defects in the NPs that were introduced by Zn and O vacancies.[39] The peaks in the green, and near red zones as observed at 528 and 600 nm, were attributed to the energy gap between the interstitial Zn conduction band and antisite O conduction band.

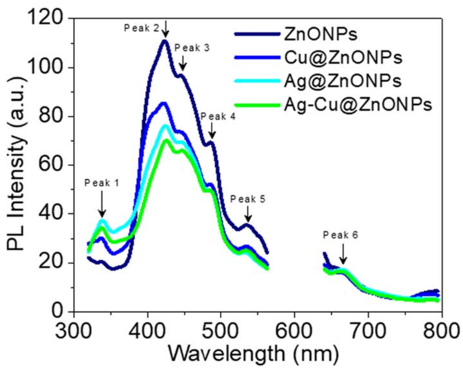

Fig. 4 PL emission spectra of undoped and doped ZnONPs at $\lambda_{ex} =$ 300 nm.

However, for the composite samples of Cu@ZnONPs, Ag@ZnONPs, and Ag–Cu@ZnONPs, the overall intensity of this main peak at 423 nm consecutively decreased with slight changes in the peak position to 421 nm, 424 nm, and 425 nm, respectively. Although the position of other peaks at 446 nm, 487 nm, and 535 nm remained the same, however, the position of 336 nm and 653 nm was changed in the doped NPs. Fang *et al.* (2018) also reported that Cu doping in ZnONPs resulted in weakened luminous intensity which was due to the increase in the non-radiation recombination process.[40] They speculated that passivation of the defect state occurred when energy from the defect emission was absorbed due to the presence of doped Cu in the lattice of ZnO. The altered intensity of the peaks suggests a significant effect on the optical properties of pure ZnO after Ag and Cu doping that might be attributed to the reduction in the band gap energy of ZnONPs.[41]

3.3 SEM, EDS, and HRTEM analyses

Morphological examination and determination of the elemental composition of NPs were carried out using field emission scanning electron microscopy (FE-SEM) and energy dispersive spectroscopy (EDS). The SEM micrographs in Fig. 5 indicate the flower-like morphology of the phytogenic ZnONPs, Ag@ZnONPs, Cu@ZnONPs, and Ag–Cu@ZnONPs where the size of flowers was 1185 nm, 955 nm, 1427 nm, and 952 nm respectively. The size of the flowers was bigger in Cu@ZnONPs where the size of the receptacle-like structure in the center and the petals were 353 nm and 550 nm, respectively while those for Ag@ZnONPs were 303 nm and 373 nm, respectively. Although the size of the whole flower in Ag–Cu@ZnONPs was identical to that of Ag@ZnONPs, the receptacle was larger (398 nm) while the petals showed comparatively smaller size (243 nm). The EDS spectra confirmed the elemental composition of the NPs that are summarized in Table 1. Besides, the other small peaks in the EDS spectra displayed the presence of some other elements like Si which was from the glass substratum, Au from the coating, and C as well as Mg that might be associated with phytochemicals present in the LFLE used during synthesis. Similarly, the presence of elemental K, Mg, Ca, and Na was noted in the EDX spectrum of ZnONPs synthesized from the *Ziziphus jujuba* fruit extract.[42]

The distribution of elemental Zn, O, Ag, and Cu was confirmed in the nanomaterials by elemental mapping of FE-SEM. Fig. 6 exhibits the field selected in FE-SEM images for the undoped and doped ZnONPs while different colors like red, green, yellow, and magenta in elemental mapping indicate Zn, O, Ag, and Cu respectively. The high density of both Zn and O compared to Ag and Cu is evident in Fig. 5. The absence of Ag or Cu was noted in the pure ZnONPs while a homogeneous distribution of Ag and Cu was noted in the doped ZnONPs. Thus, elemental mapping confirmed the successful doping of

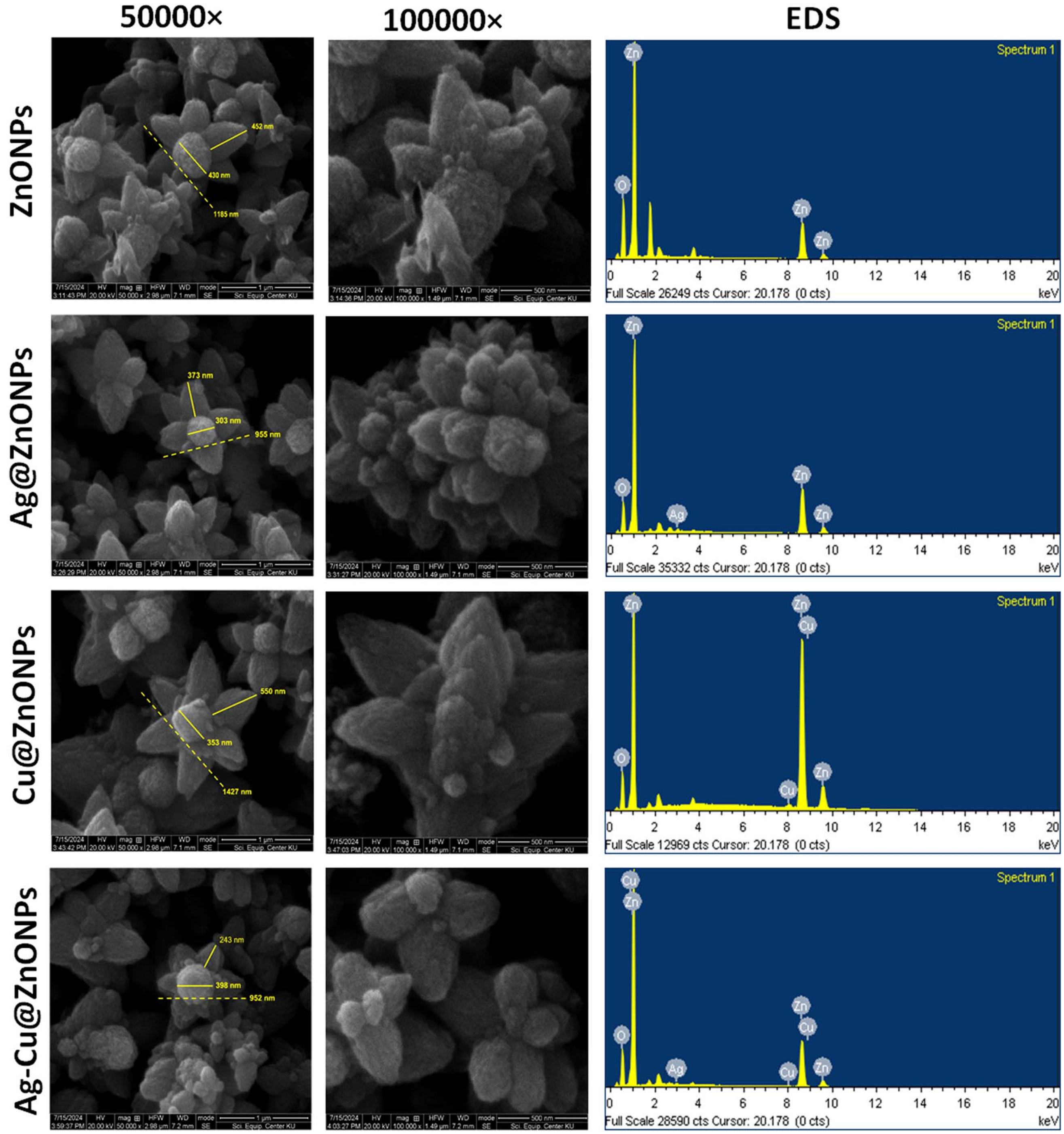

Fig. 5 FE-SEM images at different magnifications and EDS results of the undoped and doped ZnONPs.

Table 1 Elemental composition of the undoped and doped ZnONPs

	Weight%				Atomic%			
NPs	Zn	O	Ag	Cu	Zn	O	Ag	Cu
ZnONPs	68.87	31.13	—	—	35.12	64.88	—	—
Ag@ZnONPs	80.58	18.11	1.31	—	51.86	47.62	0.51	—
Cu@ZnONPs	91.54	7.14	—	1.31	74.98	23.91	—	1.11
Ag–Cu@ZnONPs	78.20	19.83	0.73	1.24	48.59	50.34	0.28	0.79

Ag and Cu in Ag–Cu@ZnONPs which is well in agreement with the EDS results. This also indicated the purity of the nanomaterials which complies with Cu/ZnONPs synthesized using the *Euphorbia prolifera* leaf extract.[43]

The morphology and structure features of the NPs were further analyzed by TEM, the results of which are shown in Fig. 7. Numerous small particles assembled to form flower-like NPs that were around 900 to 1500 nm. This might be attributed to aggregation or overlapping as observed by Saravanan *et al.*

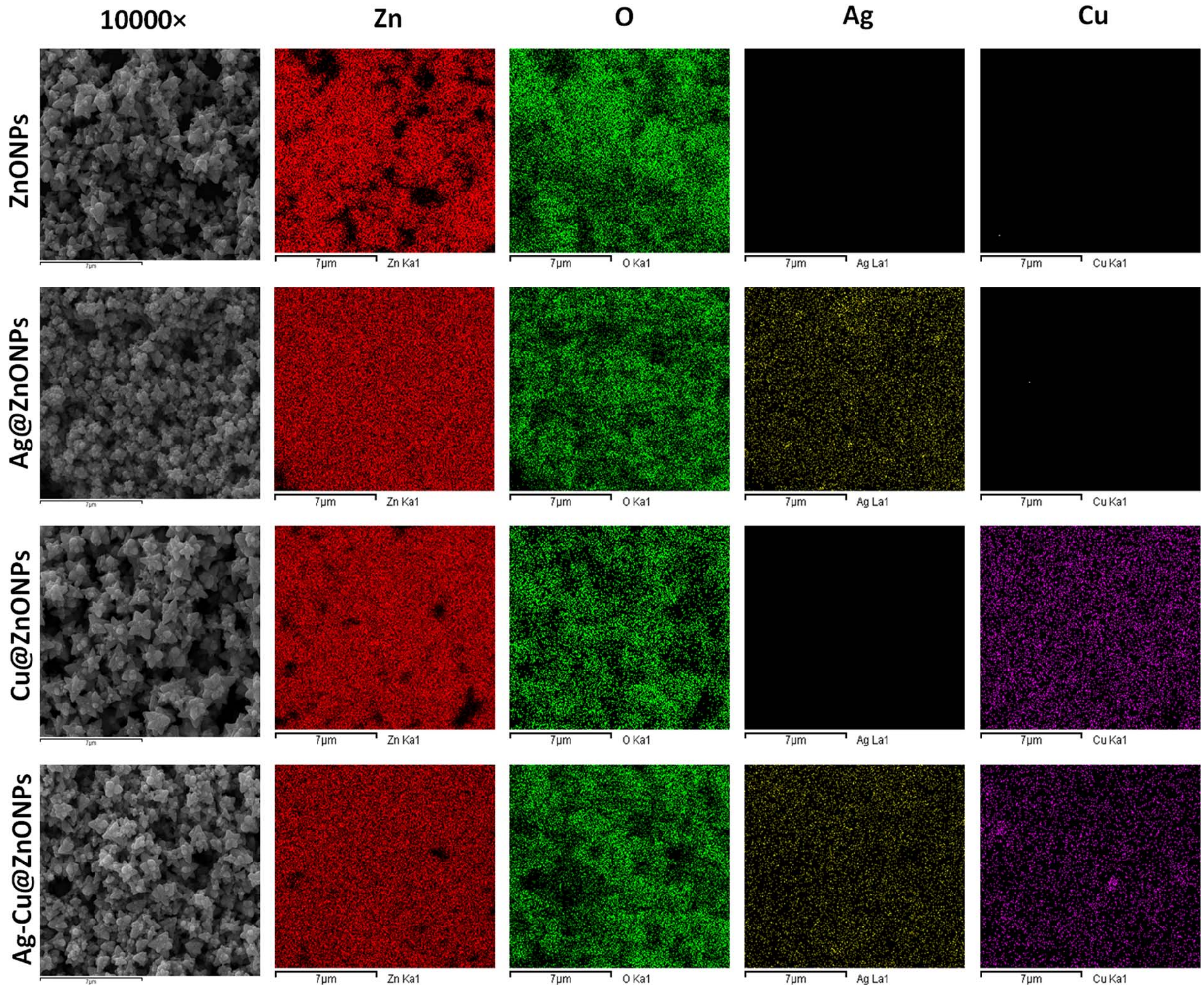

Fig. 6 Elemental mapping of Zn (red), O (green), Ag (yellow), and Cu (magenta) in the undoped and doped ZnONPs.

(2014) as well.[44] However, it is important to note that the particle morphology changed negligibly due to the incorporation of the doping agents. The high-resolution TEM (HR-TEM) image confirmed the structural uniformity among the phytogenic NPs. The *d*-spacing between two well-oriented parallel lattice fringes in ZnONPs, Ag@ZnONPs, Cu@ZnONPs, and Ag–Cu@ZnONPs is about 0.191 nm, 0.248 nm, 0.260 nm, and 0.282 nm which correspond to the (102), (101), (002), and (100) planes, respectively. Hence, the incorporation of Ag and Cu atoms into the ZnO lattice did not alter the crystal structure of ZnO unlike the observed distortions reported in Cu-doped ZnONPs fabricated using a microwave-assisted hydrothermal method.[40] The selected area electron diffraction (SAED) pattern indicated a crystalline hexagonal wurtzite structure.

3.4 Particle size, zeta potential and XRD analysis

The hydrodynamic diameters of ZnONPs, Ag@ZnONPs, Cu@ZnONPs, and Ag–Cu@ZnONPs in water are in the range from 1 µm to 3.5 µm indicating agglomeration (Fig. S1–S4†). The zeta potential of ZnONPs, Ag@ZnONPs, Cu@ZnONPs, and Ag–Cu@ZnONPs is -3.76 ± 0.14, -38.32 ± 0.45, -32.92 ± 1.00, and -26.33 ± 2.02. This indicated higher stability of the Ag@ZnONPs reflecting less aggregation and more surface area. The structural analysis of ZnONPs, Ag@ZnONPs, Cu@ZnONPs, and Ag–Cu@ZnONPs was accomplished using an X-ray diffraction spectrometer. The X-ray diffraction patterns of the pure and doped ZnONPs are shown in Fig. 8A, exhibiting various diffraction peaks corresponding to the (100), (002), (101), (102), (110), (103), (200), (112), (201), (004), and (202) planes. These characteristic peak patterns match the JCPDS file of the ZnO reference no. 01-079-0208, confirming the wurtzite hexagonal structure of ZnONPs without impurities. No additional peaks are observed in the doped ZnONPs, except for Ag@ZnONPs, which exhibited a diffraction peak at 34.16°, indicating the presence of an AgO monoclinic structure corresponding to the (002) plane in the JCPDS file no. 96-403-1661. A similar observation was reported when metals like Ag, Al, Cu, and Mn were doped in ZnONPs. The absence of Ag and Cu peaks in Cu@ZnONPs and Ag–Cu@ZnONPs suggests that Ag

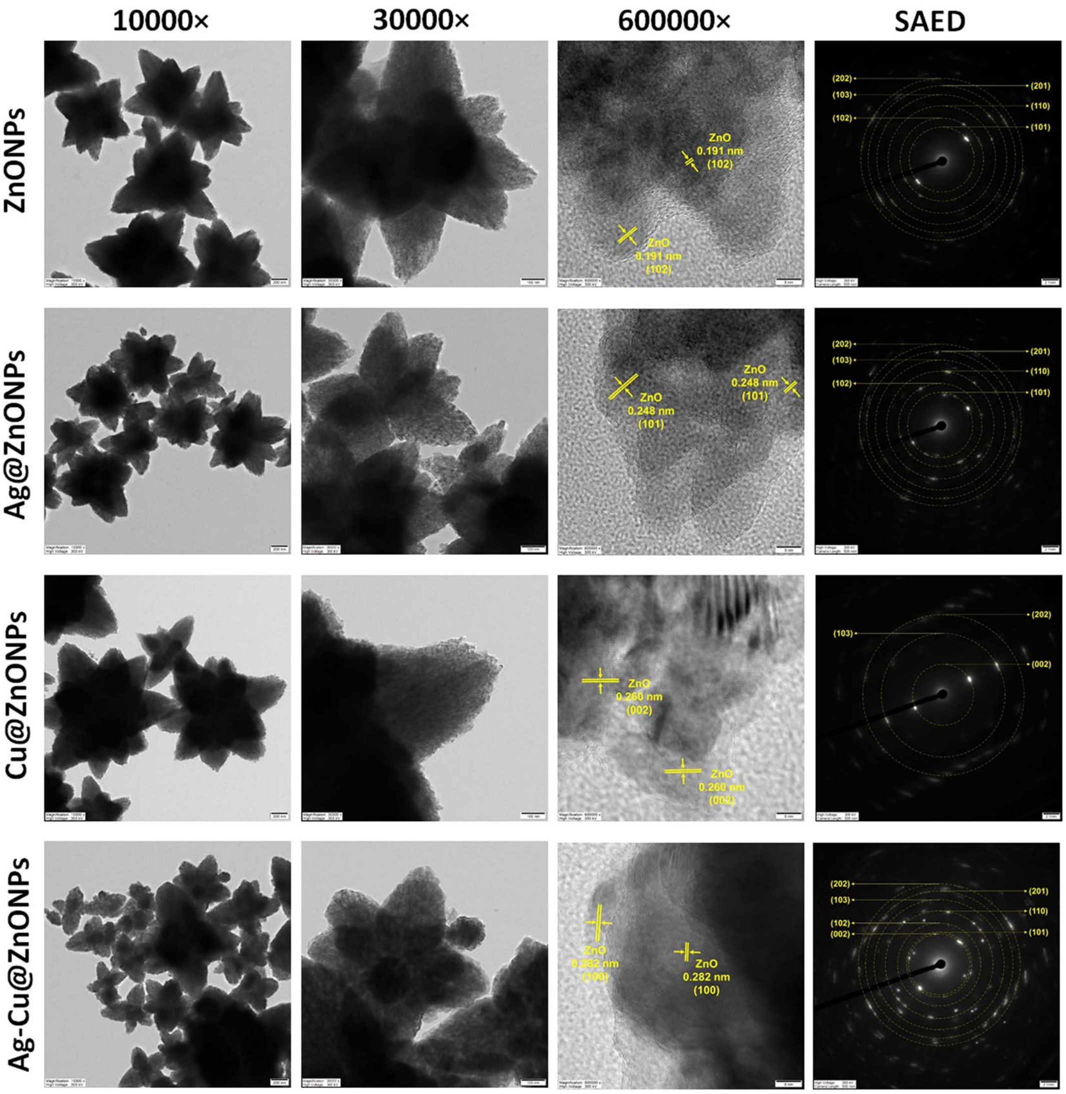

Fig. 7 HR-TEM images showing the lattice and SAED pattern of the undoped and doped ZnONPs.

and Cu are likely inserted into the ZnO lattice.[45] Fig. 8B displays the XRD shift of the doped ZnONPs compared to the pure ZnONPs at the (110) plane (2θ values shown in Table 2). A shift in the peak position is observed for Ag@ZnONPs, Cu@ZnONPs, and Ag–Cu@ZnONPs compared to ZnONPs. This shift is primarily due to the difference between the ionic radii of Ag^+ (1.22 Å), Cu^{2+} (0.73 Å), and Zn^{2+} (0.74 Å), as indicated by the difference in lattice constants upon doping shown in Table 2.[27,46]

The calculated lattice parameters, estimated from the (100) and (002) planes of the XRD pattern of the hexagonal wurtzite structure, are illustrated in Table 2. It can be seen that the lattice parameters decrease after Ag doping, which can be attributed to the relatively larger ionic radii of Ag^+ compared to Zn^{2+}.[47] Conversely, an increase in lattice parameters was observed for Cu-doped and Ag–Cu-doped ZnONPs compared to the pure ZnONPs, due to the relatively smaller ionic radii of Cu^{2+} compared to Zn^{2+}.[48] The average crystallite size of the samples ranged between 11.22 and 13.23 nm, confirming the formation of NPs. In Ag@ZnONPs, the crystallite size reduced, while it increased in Cu@ZnONPs and Ag–Cu@ZnONPs, reflecting the difference in ionic radii of Ag^+ and Cu^{2+} ions compared to Zn^{2+} ions.

3.5 FTIR analysis

The FTIR spectra of the phytogenic undoped and doped ZnONPs are shown in Fig. 9A. The peaks observed at 3300 cm^{-1} to 3400 cm^{-1} are ascribed to the H–O–H stretching vibration of water molecules present in the prepared particles.[49] The peaks observed from 3570 to 3670 cm^{-1} are slightly blue-shifted for Ag@ZnONPs, Cu@ZnONPs and Ag–Cu@ZnONPs. Bloch *et al.* (2022) also reported a similar observation which they speculated to be associated with the N–H stretch vibrations from the peptide linkages.[50] The peaks at 2965 to 2975 cm^{-1} correspond to the asymmetric stretching vibration of C–H.[51] The region from 1050 cm^{-1} to 750 cm^{-1} is identified as the fingerprint

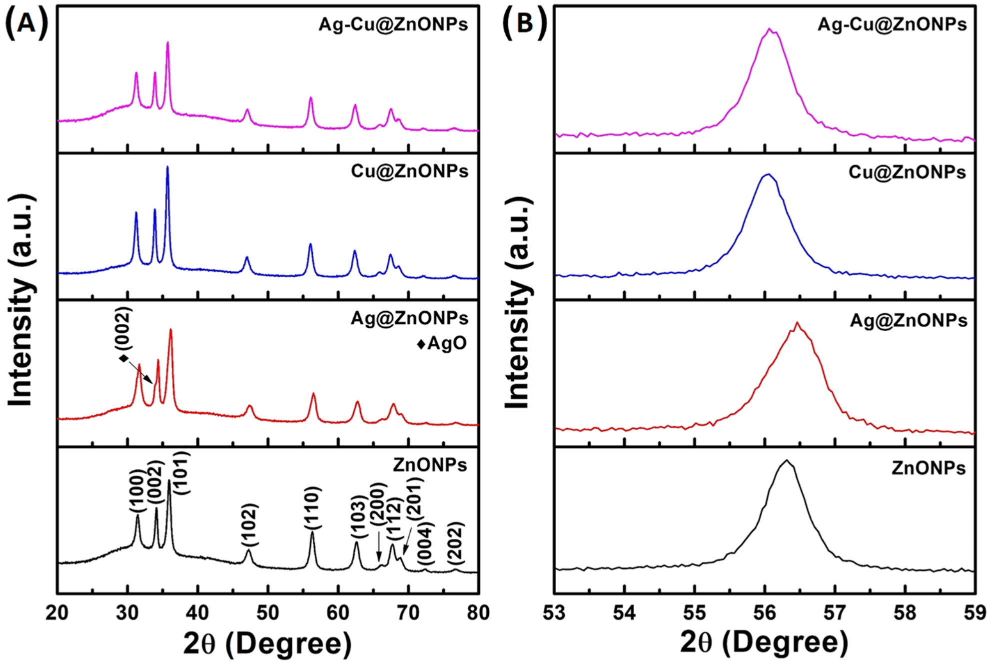

Fig. 8 XRD pattern of the (A) undoped and doped ZnONPs; (B) peak shift.

region for the alkyl group from the residual of the LFLE. The bands at 1050 cm^{-1} and 1050 cm^{-1} indicated the metal-oxide-metal modes of stretching vibrations.[52]

The FTIR spectra of the LFLE before synthesis (LFLE) and after synthesis, denoted as LELE (Ag–Cu@ZnONPs), LFLE (Cu@ZnONPs), LFLE (Ag@ZnONPs), and LFLE (ZnONPs) are presented in Fig. 9B. The FTIR spectra indicate that most functional groups in the LFLE were preserved after nanoparticle synthesis, with only minor shifts in peak positions. For example, the peak at 1637 cm^{-1} (C═C stretching) in the LFLE shifted slightly to 1554 cm^{-1} (N–H bending) in LFLE (Ag–Cu@ZnONPs), and the peak at 3740 cm^{-1} shifted to 3694 cm^{-1} (O–H stretching of free hydroxyl groups and phenolic hydroxyl groups). The shifting in the peaks was attributed to the interaction of functional groups with NPs especially the olefinic, aromatic, amines and hydroxyl groups.

3.6 Photocatalytic dye degradation

The exposure to light irradiation resulted in a change in MB dye concentration. The peak intensity at 662 nm of MB dye decreased with the light irradiation time as evident from Fig. 10A–D. Degradation of MB dye was up to 20%, 29%, 45%, and 60% when reacted with ZnONPs, Cu@ZnONPs, Ag@ZnONPs, and Ag–Cu@ZnONPs, respectively as shown in Fig. 10E. The reaction rates for the photocatalytic decomposition of MB dye fitted with the pseudo-first-order reaction kinetics. The reaction rate constant obtained from the $\ln(A_0/A_t)$ *vs.* t (time) plot, as shown in Fig. 10F was 2.2×10^{-3}, 3.8×10^{-3}, 6.4×10^{-3}, and 9.8×10^{-3} min^{-1} for ZnONPs, Cu@ZnONPs, Ag@ZnONPs, and Ag–Cu@ZnONPs, respectively.

Since the maximum photocatalytic dye degradation was exhibited by Ag–Cu@ZnONPs, the optimization studies were carried out at different pH values by varying the concentration of the NPs and MB dye. At pH 4 and pH 11 the NPs exhibited a removal efficiency of 38% and 68% with reaction rate constants equivalent to 5.0×10^{-3} and 12.8×10^{-3} min^{-1}, respectively. The degradation performance of the sample is shown in Fig. 11. A higher pH leads to an increased concentration of OH^- in the solution. This higher availability of hydroxyl ions enhances the probability of their interaction with the photogenerated holes, leading to more hydroxyl radicals. As the concentration of hydroxyl radicals increases, the rate of

Table 2 Position of the diffraction peak at the (110) plane, lattice parameter, and average crystallite size of the undoped and doped ZnONPs

		Lattice parameter (nm)			
NPs	ZnO (110) peak position (°)	*a*	*c*	*c*/*a*	Average crystallite size (nm)
ZnONPs	56.32	0.3282	0.5254	1.6010	12.75
Ag@ZnONPs	56.46	0.3260	0.5217	1.6000	11.22
Cu@ZnONPs	56.05	0.3306	0.5285	1.5986	13.14
Ag–Cu@ZnONPs	56.07	0.3304	0.5279	1.5978	13.23

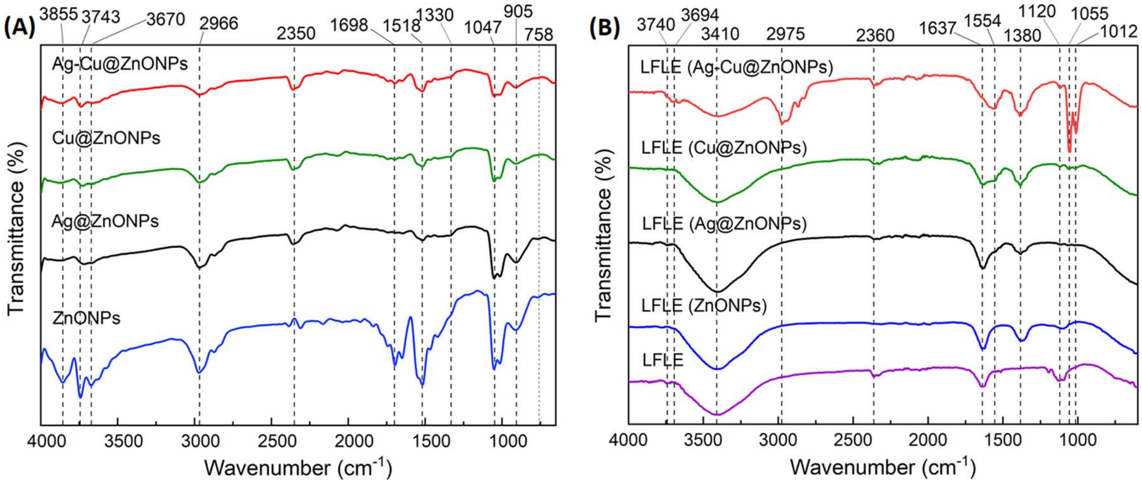

Fig. 9 FTIR spectra of the (A) undoped and doped ZnONPs; (B) LFLE before and after synthesis of NPs.

degradation of the dye through the oxidative process also increases. So, at a higher pH value that is at pH 11 the Ag–Cu@ZnONPs showed higher degradation efficiency.

At a NP concentration of 0.3 g L^{-1} and 0.5 g L^{-1} they showed a degradation efficiency of 46% and 67% with reaction rate constants equivalent to 6.9 × 10^{-3} and, 12.8 × 10^{-3} min^{-1}, respectively. The high concentration of catalysts leads to the greater overall surface area available for dye molecules to interact and adsorb onto. The photocatalysts work by the principle of absorbing light to create e–h pairs that drive the degradation of dye molecules. Thus, with the higher concentration of catalysts, more particles are available to absorb the incident light, leading to the greater generation of e–h pairs which accelerates the dye degradation process. The Ag–

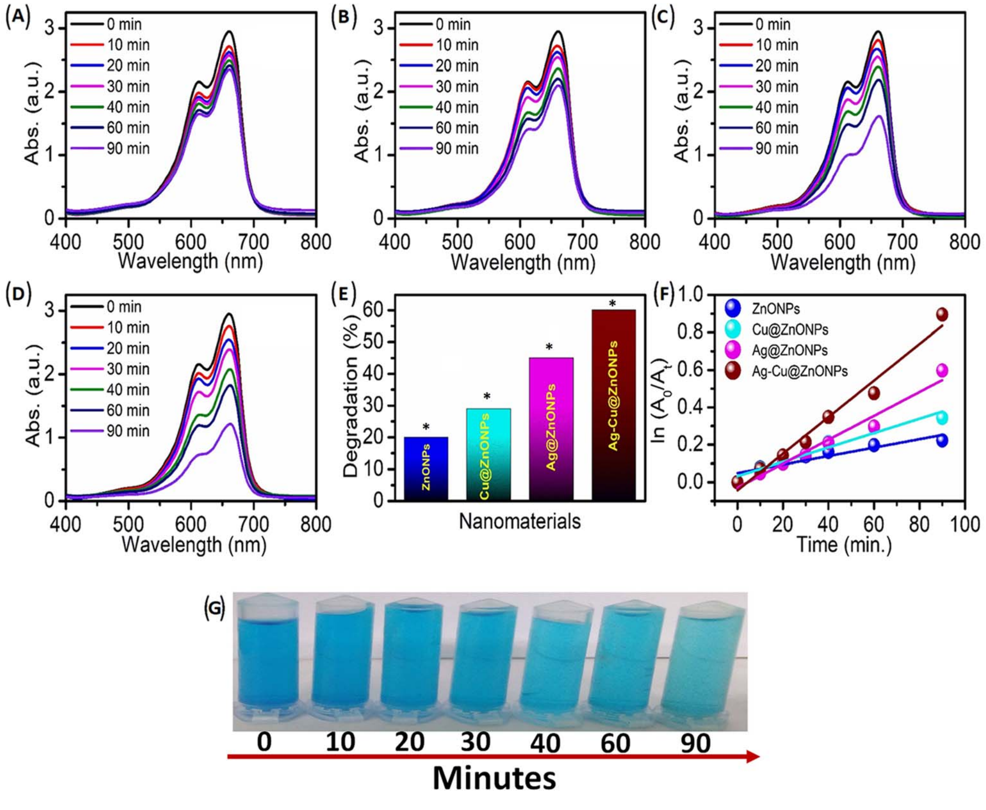

Fig. 10 Photocatalytic MB dye degradation by (A) ZnONPs; (B) Ag@ZnONPs; (C) Cu@ZnONPs; and (D) Ag–Cu@ZnONPs; (E) degradation efficiency; and (F) pseudo-first-order kinetic constant of synthesized NPs; (G) representative digital picture of MB dye degradation under visible light from 0 to 90 min. *$p < 0.05$; the mean difference in the photocatalytic degradation is found to be significant among the NPs and the time points at the 0.05 level by two factor ANOVA.

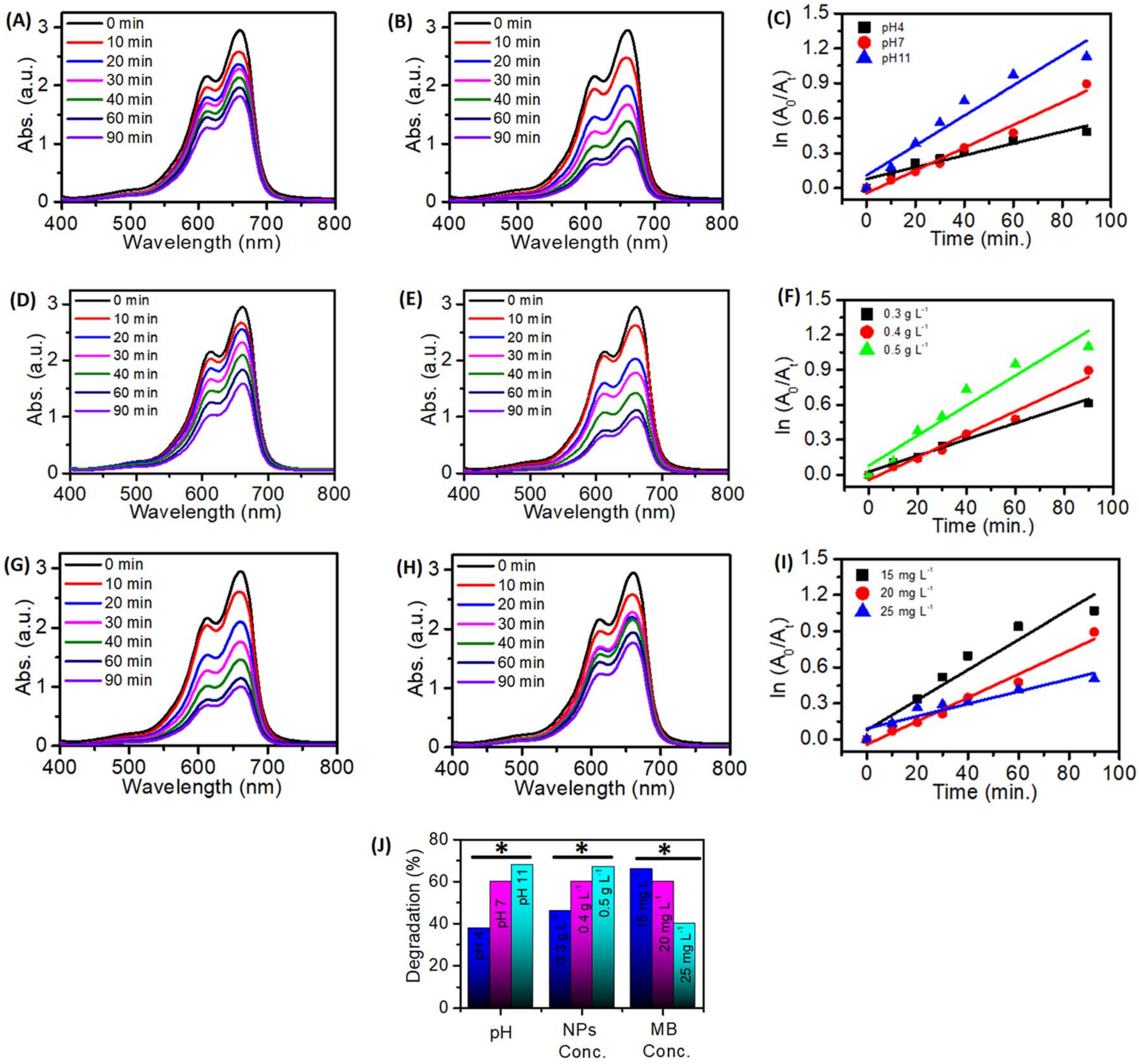

Fig. 11 Photocatalytic dye degradation by Ag–Cu@ZnONPs under various reaction conditions: (A) pH 4 and (B) pH 11 with an Ag–Cu@ZnONP concentration of 0.4 g L^{-1} & MB concentration of 20 mg L^{-1}; (C) pseudo-first-order kinetic constant at various pH values; (D) 0.3 g L^{-1}; and (E) 0.5 g L^{-1} of Ag–Cu@ZnONPs with the MB concentration fixed at 20 mg L^{-1}; (F) pseudo-first-order kinetic constant at various Ag–Cu@ZnONP concentrations; (G) 15 mg L^{-1} and (H) 25 mg L^{-1} MB concentration with the Ag–Cu@ZnONP concentration fixed at 0.4 g L^{-1}; (I) pseudo-first-order kinetic constant at various MB concentrations; (J) percentage degradation of MB dye at different pH values, and Ag–Cu@ZnONP and MB concentrations. *$p < 0.05$; the mean difference in the photocatalytic degradation is found to be significant among the pH, concentration of NPs, concentration of MB dye, and the time points at the 0.05 level by two factor ANOVA.

Cu@ZnONPs exhibited a degradation efficiency of 66% and 40% with reaction rate constants of 12.5×10^{-3} and 5.1×10^{-3} min^{-1} at MB concentrations of 15 mg L^{-1} and 25 mg L^{-1}, respectively.

The observations are comparable to previous reports. Golmohammadi *et al.* (2020) reported 92% and 86% photocatalytic degradation of MB and Eriochrome Black-T, respectively, by phytogenic ZnONPs after exposure to light for 5 h which is longer than the current study.[42] Hence, it is evident that the degradation efficiency is a function of reaction time.

The effect of a free radical scavenger, EDTA-2Na at 1 mM concentration was also analyzed on MB dye degradation. Fig. 12 shows the strong inhibitory effect of EDTA-2Na on the dye degradation process. The ZnONPs, Cu@ZnONPs, Ag@ZnONPs, and Ag–Cu@ZnONPs exhibited 5, 4, 3.5, and 3% MB dye degradation with reaction rate constants of 4.28×10^{-4}, 4.27×10^{-4}, 4.12×10^{-4}, and 3.22×10^{-4} min^{-1}, respectively. This confirmed the role of ROS in the MB dye degradation process as schematically depicted in Fig. 13. This is in agreement with the earlier report on photocatalytic degradation of MB and methyl orange dyes using Au cube-ZnO core–shell NPs.[53]

In a similar study, Karthik *et al.* (2022) found enhanced degradation of MB, indigo carmine, and rhodamine B dyes after doping ZnONPs with Cu.[11] They speculated that the incorporation of the dopants into ZnONPs resulted in the extension of the light absorption range due to the generation of additional energy levels between the valence band (VB) and conduction band (CB). Thus, simultaneous doping with both Ag and Cu in

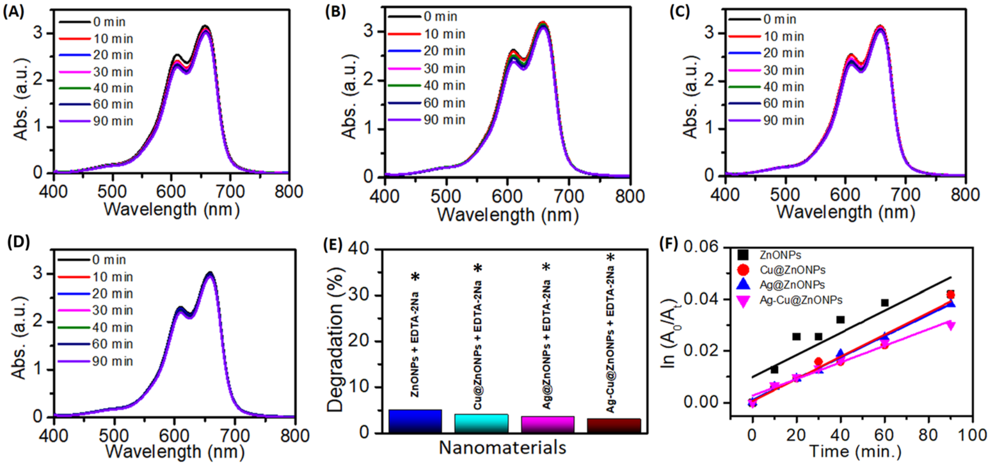

Fig. 12 Photocatalytic dye degradation in the presence of free radical scavenger EDTA-2Na by (A) ZnONPs; (B) Cu@ZnONPs; (C) Ag@ZnONPs; and (D) Ag–Cu@ZnONPs; (E) degradation efficiency; and (F) pseudo-first-order kinetic constant of synthesized NPs. $*p < 0.05$; the mean difference in the inhibition of photocatalytic degradation in the presence of EDTA-2Na is found to be significant among the NPs, and the time points at the 0.05 level by two factor ANOVA.

the current study might have created higher defect levels in ZnO that served as traps of e^-. This substantially decreased the recombination rate promoting rapid active radical formation. Ebrahimi *et al.* (2019) obtained 24% Direct Blue 15 dye degradation by Ag–Cu-doped ZnONPs under ultraviolet light after 120 min which was lower compared to that in the present work.[54] Overall, these results suggest the superior photocatalytic performance of the phytogenic NPs.

3.7 Antibacterial synergy

The standard well diffusion method was employed for qualitative estimation of the antibacterial activity of the NPs against *B. subtilis*, *S. aureus*, and *P. aeruginosa* as shown in Fig. 14. Ag@ZnONPs exhibited a ZOI up to 10 mm, 10 mm, and 11 mm against the three aforementioned bacteria, respectively, while both ZnONPs and Cu@ZnONPs showed no inhibition. The maximum ZOI of 12 mm was noted against *P. aeruginosa* followed by 9 mm against *B. subtilis* when treated with Ag–Cu@ZnONPs. Similar enhanced activity in Ag-doped ZnONPs was also reported earlier against *Escherichia coli*, *Salmonella typhi*, and *S. aureus* bacteria.[55] They speculated that lower activity against Gram-negative bacteria might be due to the presence of an additional outer lipopolysaccharide (LPS) membrane that may hinder the penetration of the NPs into the cells. Iqbal *et al.* (2015) observed that NPs with smaller grain sizes had more bactericidal effects.[56] So doping with Cu resulted in reduced antibacterial activity against multidrug-resistant *S.*

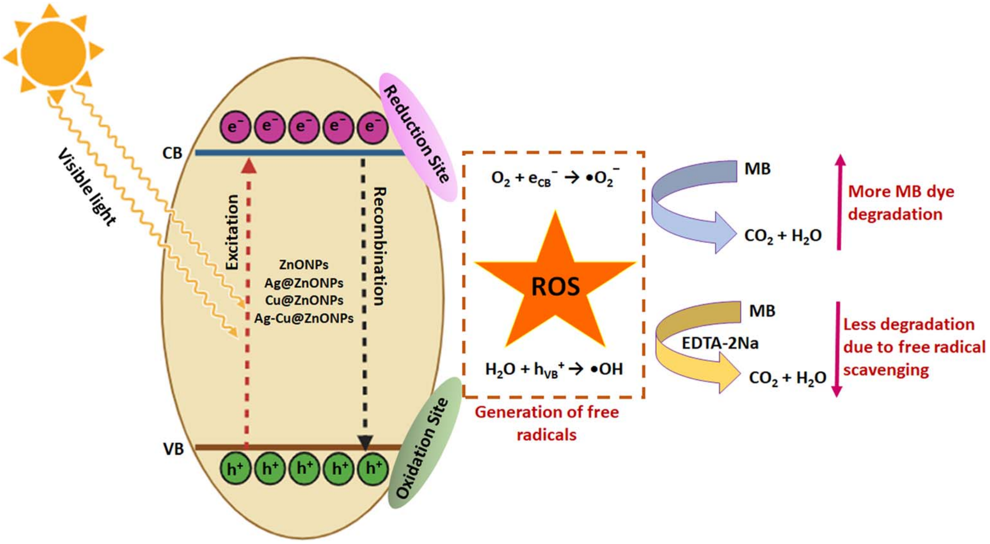

Fig. 13 Schematic representation of the reaction mechanism of MB dye degradation using undoped and doped ZnONPs in the absence and in the presence of a free radical scavenger.

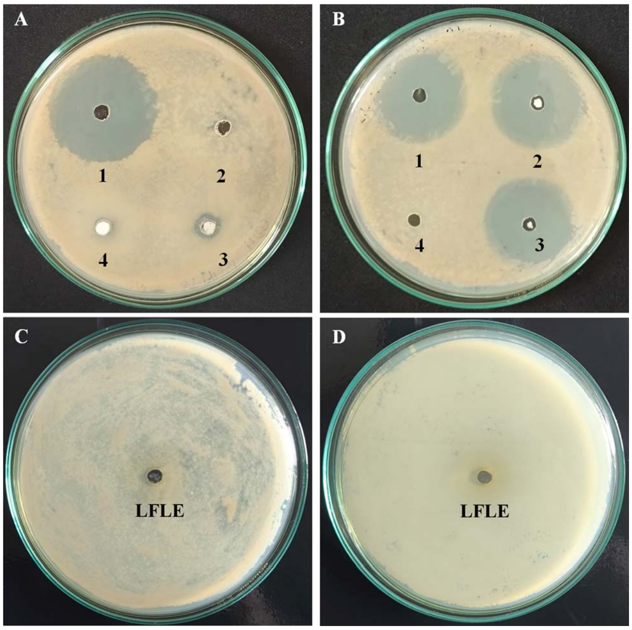

Fig. 14 Antibacterial activity. (A) representative image showing the ZOI against *B. subtilis* where 1, 2, 3, and 4 are streptomycin (positive control), water (negative control), Ag@ZnONPs, and ZnONPs, respectively; (B) antibacterial synergy with streptomycin against *B. subtilis* where 1, 2, 3, and 4 are streptomycin, ZnONPs with streptomycin, Ag@ZnONPs with streptomycin, and water, respectively; representative image of the LFLE showing no inhibition against (C) *B. subtilis* and (D) *S. aureus*.

aureus. This observation provides a strong rationale behind the higher activity of Ag@ZnONPs in the current study as it has the smallest crystallite size as evident from Table 2. Thus, this is clear evidence that the antibacterial properties of the metal oxide NPs are inversely proportional to the particle size.[31] The LFLE didn't show any antibacterial activity as evident from Fig. 14C.

The synergistic enhancement of the ZOI against bacteria treated with a combination of antibiotics and the NPs was expressed as a fold increase which is tabulated in Table 3. The highest synergy was seen with ampicillin where Ag@ZnONPs and Ag–Cu@ZnONPs exhibited a 3.84 and 3.00-fold increase in the ZOI against *P. aeruginosa*. ZnONPs showed 0.28 and 0.22-fold increases in the activity of novobiocin and streptomycin, respectively, against *S. aureus*. Cu@ZnONPs exhibited 0.22 and 0.13-fold increases in the activity of streptomycin and novobiocin against *S. aureus* and *P. aeruginosa*, respectively.

The plausible mechanisms behind the antibacterial activity of the NPs are pictorially presented in Fig. 15. The doped ZnONPs can release Zn^{2+}, Ag^{+}, and Cu^{2+} ions in the aqueous suspension. These ions along with the NPs can enter the bacterial cells and generate reactive oxygen species (ROS) that damage the DNA, vital enzymes, cellular proteins, and ribosomes.[57] The resulting oxidative stress can also disrupt the cell membrane, electron transport, and energy generation, and cause leakage of the cellular components, eventually killing the bacterial cell.[58]

Table 3 Fold increase in the ZOI (mm) of different antibiotics against bacteria in combination with undoped and doped ZnONPs[a]

	B. subtilis[b]									*S. aureus*[b]									*P. aeruginosa*[b]								
	Ampicillin			Novobiocin			Streptomycin			Ampicillin			Novobiocin			Streptomycin			Ampicillin			Novobiocin			Streptomycin		
NPs	*A*	*B*	*C*	*A*	*B*	*C*	*A*	*B*	*C*	*A*	*B*	*C*	*A*	*B*	*C*	*A*	*B*	*C*	*A*	*B*	*C*	*A*	*B*	*C*	*A*	*B*	*C*
ZnONPs	42	44	0.09	32	33	0.06	25	27	0.16	48	5	ND	30	34	0.28	19	21	0.22	5	5	0.00	20	15	ND	17	18	0.12
Ag@ZnONPs	42	43	0.04	32	32	0.00	25	26	0.08	48	5	ND	30	33	0.21	19	20	0.10	5	11	3.84	20	20	0.00	17	18	0.12
Cu@ZnONPs	38	40	0.10	31	32	0.06	30	30	0.00	46	5	ND	33	34	0.06	19	21	0.22	5	5	0.00	15	16	0.13	18	18	0.00
Ag–Cu@ZnONPs	38	38	0.00	31	31	0.00	30	32	0.13	46	5	ND	33	33	0.00	19	20	0.10	5	10	3.00	15	17	0.28	18	18	0.00

[a] Fold increases (*C*) for different antibiotics against the three bacteria were calculated as $(B^2 - A^2)/A^2$, where *A* and *B* are the ZOI in mm for antibiotic only and antibiotic in combination with NPs, respectively. In the absence of a ZOI, the well diameter (5 mm) was used to calculate (*C*). ND: not determined. [b] $p < 0.05$; the mean difference in the synergy is found to be significant among the bacteria at the 0.05 level by two factor ANOVA.

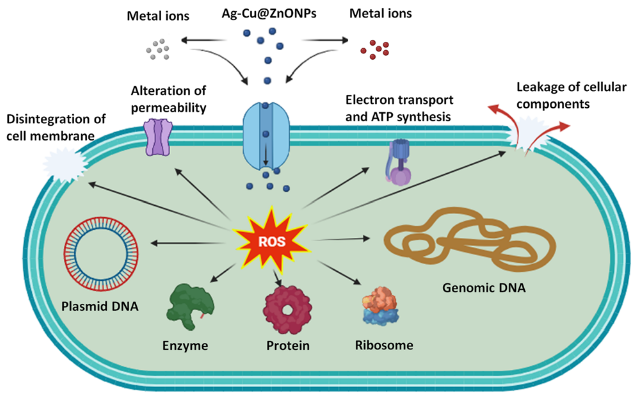

Fig. 15 Pictorial representation of the mechanism behind antibacterial activity of undoped and doped ZnONPs.

4. Conclusion

This is the first report on phytofabrication of the ZnO nanoflower using the LFLE which is a rare and unique advancement in the field. This process is rapid, efficient, simple, low-cost, and eco-friendly. The major findings of this work are presented most comprehensively with elaborate discussion and comparison with earlier reports. The present work demonstrates an environmentally benign green route to synthesize exotic flower-shaped ZnONPs and Ag/Cu-doped ZnONPs using *Leucophyllum frutescens* leaf extracts. This is a one-pot, rapid, efficient, and economical process for NP synthesis. The phytochemicals present in the extract such as phenolics and flavonoids played a key role in the synthesis and stabilization of the NPs. The UV-vis spectra confirmed successful synthesis, while the energy bandgap decreased in the doped ZnONPs. Ag@ZnONPs with smaller dimensions than Cu@ZnONPs showed higher photocatalytic dye degradation and antibacterial effects. Thus, this study provides strong evidence that the properties of NPs are size-dependent. The main challenge in biogenic synthesis is the control of shape and size where polydispersed anisotropic NPs are formed. However, the current study confirming uniform flower-like NPs as evident from the electron micrographs establishes this method as the most reliable biogenic synthesis. The EDS and elemental mapping confirmed the successful doping while XRD analysis indicated the crystalline nature. Superior photocatalytic degradation of MB and antibacterial synergy with antibiotics suggests that the phytogenic undoped and doped ZnONPs can be useful as agents for environmental remediation and infection control. Thus, there is wide scope in the future to develop membrane filters incorporating these superior nanomaterials for simultaneous removal of dyes and infectious pathogens.

Data availability

Data are available upon reasonable request.

Conflicts of interest

There are no conflicts to declare.

Acknowledgements

Pranav Pandya is thankful to the Council of Scientific and Industrial Research (CSIR, Government of India) for a Junior Research Fellowship (JRF) (09/1371(15459)/2022-EMR-I). Dr Sougata Ghosh is thankful to the Program Management Unit for Human Resources & Institutional Development and Innovation (PMU-B) for granting a proposal entitled "Post-Doctoral Research Competency Enhancement Program for carbon recycling based on metal oxide graphene-liked nanosheet photocatalysts" under the Program of the National Postdoctoral and Postgraduate System approved by PMU-B Board Committees (Contract No. B13F670067) dated 23rd February, 2024.

References

1 R. Revathy, J. Joseph, C. Augustine, T. Sajini and B. Mathew, Synthesis and catalytic applications of silver nanoparticles: A sustainable chemical approach using indigenous reducing and capping agents from *Hyptis capitata*, *Environ. Sci.: Adv.*, 2022, **1**, 491–505, DOI: **10.1039/D2VA00044J**.

2 A. K. Shimi, C. Parvathiraj, S. Kumari, J. Dalal, V. Kumar, S. M. Wabaidur and Z. A. Alothman, Green synthesis of SrO nanoparticles using leaf extract of *Albizia julibrissin* and its recyclable photocatalytic activity: An eco-friendly approach for treatment of industrial wastewater, *Environ. Sci.: Adv.*, 2022, **1**, 849–861, DOI: **10.1039/D2VA00018K**.

3 H. Agarwal, S. Venkat Kumar and S. Rajeshkumar, A review on green synthesis of zinc oxide nanoparticles –An eco-friendly approach, *Resour.-Effic. Technol.*, 2017, **3**, 406–413, DOI: **10.1016/j.reffit.2017.03.002**.

4 A. Sirelkhatim, S. Mahmud, A. Seeni, N. H. M. Kaus, L. C. Ann, S. K. M. Bakhori, H. Hasan and D. Mohamad, Review on zinc oxide nanoparticles: Antibacterial activity and toxicity mechanism, *Nano-Micro Lett.*, 2015, **7**, 219–242, DOI: **10.1007/s40820-015-0040-x**.

5 C. Pushpalatha, J. Suresh, V. S. Gayathri, S. V. Sowmya, D. Augustine, A. Alamoudi, B. Zidane, N. H. Mohammad Albar and S. Patil, Zinc oxide nanoparticles: A review on its applications in dentistry, *Front. Bioeng. Biotechnol.*, 2022, **10**, 917990, DOI: **10.3389/fbioe.2022.917990**.

6 O. Lupan, V. Cretu, V. Postica, M. Ahmadi, B. R. Cuenya, L. Chow, I. Tiginyanu, B. Viana, T. Pauporte and R. Adelung, Silver-doped zinc oxide single nanowire multifunctional nanosensor with a significant enhancement in response, *Sens. Actuators, B*, 2016, **223**, 893–903, DOI: **10.1016/j.snb.2015.10.002**.

7 E. Mosquera, C. Rojas-Michea, M. Morel, F. Gracia, V. Fuenzalida and R. A. Zárate, Zinc oxide nanoparticles with incorporated silver: Structural, morphological, optical and vibrational properties, *Appl. Surf. Sci.*, 2015, **347**, 561–568, DOI: **10.1016/j.apsusc.2015.04.148**.

8 Swati, R. Verma, A. Chauhan, M. Shandilya, X. Li, R. Kumar and S. Kulshrestha, Antimicrobial potential of Ag-doped ZnO nanostructure synthesized by the green method using *Moringa oleifera* extract, *J. Environ. Chem. Eng.*, 2020, **8**, 103730, DOI: **10.1016/j.jece.2020.103730**.

9 M. Benamara, K. Iben Nassar, P. Rivero-Antúnez, M. Essid, S. Soreto Teixeira, S. Zhao, A. Serrà and L. Esquivias, Study of electrical and dielectric behaviors of copper-doped zinc oxide ceramic prepared by spark plasma sintering for electronic device applications, *Nanomaterials*, 2024, **14**(5), 402, DOI: **10.3390/nano14050402**.

10 J. Zhang, Y. Dong, J. Yao, M. Zhai, M. Zhu, G. Wang, J. Li, P. F. Ferrari and B. Liu, Copper doping and oxygen vacancy synergistic modification of zinc oxide nanosheets: Significantly improved antibacterial properties, *Mater. Lett.*, 2024, **369**, 136777, DOI: **10.1016/j.matlet.2024.136777**.

11 K. V. Karthik, A. V. Raghu, K. R. Reddy, R. Ravishankar, M. Sangeeta, N. P. Shetti and C. V. Reddy, Green synthesis of Cu-doped ZnO nanoparticles and its application for the photocatalytic degradation of hazardous organic pollutants, *Chemosphere*, 2022, **287**, 132081, DOI: **10.1016/j.chemosphere.2021.132081**.

12 E. L. Irede, R. F. Awoyemi, B. Owolabi, O. R. Aworinde, R. O. Kajola, A. Hazeez, A. A. Raji, L. O. Ganiyu, C. O. Onukwuli, A. P. Onivefu and I. H. Ifijen, Cutting-edge developments in zinc oxide nanoparticles: Synthesis and applications for enhanced antimicrobial and UV protection in healthcare solutions, *RSC Adv.*, 2024, **14**(29), 20992–21034, DOI: **10.1039/D4RA02452D**.

13 R. T. Hussain, M. S. Hossain and J. H. Shariffuddin, Green synthesis and photocatalytic insights: A review of zinc oxide nanoparticles in wastewater treatment, *Materials Today Sustainability*, 2024, **26**, 100764, DOI: **10.1016/j.mtsust.2024.100764**.

14 B. Abebe, B. Kefale and D. T. Leku, Synthesis of copper–silver–zinc oxide nanocomposites for 4-nitrophenol reduction: Doping and heterojunction, *RSC Adv.*, 2023, **13**, 4523–4529, DOI: **10.1039/D2RA07845G**.

15 O. A. Jaramillo-Morales, E. Díaz-Cervantes, L. D. Via, A. N. Garcia-Argaez, J. V. Espinosa-Juárez, J. C. Ovando-Zambrano, V. M. Munoz-Perez, C. Valadez-Vega and M. Bautista, Hepatoprotective activity, in silico analysis, and molecular docking study of verbascoside from *Leucophyllum frutescens* in rats with post-necrotic liver damage, *Sci. Pharm.*, 2023, **91**, 40, DOI: **10.3390/scipharm91030040**.

16 B. Gami, K. Bloch, S. M. Mohammed, S. Karmakar, S. Shukla, A. Asok, S. Thongmee and S. Ghosh, *Leucophyllum frutescens* mediated synthesis of silver and gold nanoparticles for catalytic dye degradation, *Front. Chem.*, 2022, **10**, 932416, DOI: **10.3389/fchem.2022.932416**.

17 C. J. Martínez-Rivas, R. Álvarez-Román, C. Rivas-Morales, A. Elaissari, H. Fessi and S. A. Galindo-Rodríguez, Quantitative aspect of *Leucophyllum frutescens* fraction before and after encapsulation in polymeric nanoparticles, *J. Anal. Methods Chem.*, 2017, **2017**, 9086467, DOI: **10.1155/2017/9086467**.

18 A. A. Thabet, I. M. Ayoub, F. S. Youssef, E. Al Sayed and A. N. B. Singab, Essential oils from the leaves and flowers of *Leucophyllum frutescens* (Scrophulariaceae): Phytochemical analysis and inhibitory effects against elastase and collagenase in vitro, *Nat. Prod. Res.*, 2022, **36**, 4698–4702, DOI: **10.1080/14786419.2021.2000981**.

19 S. Chu, L. Xian, C. Lai, W. Yang, J. Wang, M. Long, J. Ouyang, D. Liao and S. Zeng, Migration and risks of potentially toxic elements from sewage sludge applied to acid forest soil, *J. For. Res.*, 2023, **34**(6), 2011–2026, DOI: **10.1007/s11676-023-01621-6**.

20 K. Singh, Nancy, M. Bhattu, G. Singh, N. M. Mubarak and J. Singh, Light-absorption-driven photocatalysis and antimicrobial potential of PVP-capped zinc oxide nanoparticles, *Sci. Rep.*, 2023, **13**(1), 13886, DOI: **10.1038/s41598-023-41103-7**.

21 S. S. Wagh, V. S. Kadam, C. V. Jagtap, D. B. Salunkhe, R. S. Patil, H. M. Pathan and S. P. Patole, Comparative studies on synthesis, characterization and photocatalytic activity of Ag doped ZnO nanoparticles, *ACS Omega*, 2023, **8**, 7779–7790, DOI: **10.1021/acsomega.2c07499**.

22 S. Ghosh, S. Patil, M. Ahire, R. Kitture, S. Kale, K. Pardesi, S. S. Cameotra, J. Bellare, D. D. Dhavale, A. Jabgunde and B. A. Chopade, Synthesis of silver nanoparticles using *Dioscorea bulbifera* tuber extract and evaluation of its synergistic potential in combination with antimicrobial agents, *Int. J. Nanomed.*, 2012, **7**, 483–496, DOI: **10.2147/IJN.S24793**.

23 H. H. Basri, R. A. Talib, R. Sukor, S. H. Othman and H. Ariffin, Effect of synthesis temperature on the size of ZnO nanoparticles derived from pineapple peel extract and antibacterial activity of ZnO–starch nanocomposite films, *Nanomaterials*, 2020, **10**, 1061, DOI: **10.3390/nano10061061**.

24 W. Zhu, C. Hu, Y. Ren, Y. Lu, Y. Song, Y. Ji, C. Han and J. He, Green synthesis of zinc oxide nanoparticles using *Cinnamomum camphora* (L.) Presl leaf extracts and its antifungal activity, *J. Environ. Chem. Eng.*, 2021, **9**, 106659, DOI: **10.1016/j.jece.2021.106659**.

25 K. R. Basavalingiah, S. Harishkumar, Udayabhanu, G. Nagaraju, D. Rangappa and Chikkahanumantharayappa, Highly porous, honeycomb like Ag–ZnO nanomaterials for enhanced photocatalytic and photoluminescence studies: green synthesis using *Azadirachta indica* gum, *SN Appl. Sci.*, 2019, **1**, 935, DOI: **10.1007/s42452-019-0863-z**.

26 A. Rahman, A. L. Tan, M. H. Harunsani, N. Ahmad, M. Hojamberdiev and M. M. Khan, Visible light induced antibacterial and antioxidant studies of ZnO and Cu-doped ZnO fabricated using aqueous leaf extract of *Ziziphus mauritiana* Lam, *J. Environ. Chem. Eng.*, 2021, **9**, 105481, DOI: **10.1016/j.jece.2021.105481**.

27 M. H. Rashid, S. I. Sujoy, M. S. Rahman and M. J. Haque, *Aloe vera* assisted green synthesis of Ag and Cu co-doped ZnO nanoparticles and a comprehensive analysis of their structural, morphological, optical, electrical and antibacterial properties, *Heliyon*, 2024, **10**, E25438, DOI: **10.1016/j.heliyon.2024.e25438**.

28 S. Vijayakumar, C. Krishnakumar, P. Arulmozhi, S. Mahadevan and N. Parameswari, Biosynthesis, characterization and antimicrobial activities of zinc oxide nanoparticles from leaf extract of *Glycosmis pentaphylla*

(Retz.) DC, *Microb. Pathog.*, 2018, **116**, 44–48, DOI: 10.1016/j.micpath.2018.01.003.

29 S. Sharma, K. Kumar, N. Thakur, S. Chauhan and M. S. Chauhan, The effect of shape and size of ZnO nanoparticles on their antimicrobial and photocatalytic activities: a green approach, *Bull. Mater. Sci.*, 2020, **43**, 20, DOI: 10.1007/s12034-019-1986-y.

30 S. Ghosh, V. S. Goudar, K. G. Padmalekha, S. V. Bhat, S. S. Indi and H. N. Vasan, ZnO/Ag nanohybrid: Synthesis, characterization, synergistic antibacterial activity and its mechanism, *RSC Adv.*, 2012, **2**, 930–940, DOI: 10.1039/C1RA00815C.

31 M. D. Jayappa, C. K. Ramaiah, M. A. P. Kumar, D. Suresh, A. Prabhu, R. P. Devasya and S. Sheikh, Green synthesis of zinc oxide nanoparticles from the leaf, stem and in vitro grown callus of *Mussaenda frondosa* L.: Characterization and their applications, *Appl. Nanosci.*, 2020, **10**, 3057–3074, DOI: 10.1007/s13204-020-01382-2.

32 H. Padalia and S. Chanda, Characterization, antifungal and cytotoxic evaluation of green synthesized zinc oxide nanoparticles using *Ziziphus nummularia* leaf extract, *Artif. Cells, Nanomed., Biotechnol.*, 2017, **45**, 1751–1761, DOI: 10.1080/21691401.2017.1282868.

33 W. Muhammad, N. Ullah, M. Haroon and B. H. Abbasi, Optical, morphological and biological analysis of zinc oxide nanoparticles (ZnO NPs) using *Papaver somniferum* L, *RSC Adv.*, 2019, **9**, 29541–29548, DOI: 10.1039/C9RA04424H.

34 M. B. Islam, M. J. Haque, N. M. Shehab and M. S. Rahman, Synthesis and characterization (optical and antibacterial) of silver doped zinc oxide nanoparticles, *Open Ceram.*, 2023, **14**, 100370, DOI: 10.1016/j.oceram.2023.100370.

35 M. M. Khan, M. H. Harunsani, A. L. Tan, M. Hojamberdiev, Y. A. Poi and N. Ahmad, Antibacterial studies of ZnO and Cu-doped ZnO nanoparticles synthesized using aqueous leaf extract of *Stachytarpheta jamaicensis*, *BioNanoScience*, 2020, **10**, 1037–1048, DOI: 10.1007/s12668-020-00775-5.

36 R. Elilarassi and G. Chandrasekaran, Structural, optical and magnetic characterization of Cu-doped ZnO nanoparticles synthesized using solid state reaction method, *J. Mater. Sci.: Mater. Electron.*, 2009, **21**, 1168–1173, DOI: 10.1007/s10854-009-0041-y.

37 M. Gangarapu, S. Sarangapany, D. P. Suja and V. B. R. Arava, Highly recyclable and ultra-rapid catalytic reduction of organic pollutants on Ag–Cu@ ZnO bimetal nanocomposite synthesized via green technology, *Appl. Nanosci.*, 2018, **8**, 1123–1131, DOI: 10.1007/s13204-018-0753-5.

38 S. Arya, P. K. Lehana and S. B. Rana, Synthesis of zinc oxide nanoparticles and their morphological, optical, and electrical characterizations, *J. Electron. Mater.*, 2017, **46**, 4604–4611, DOI: 10.1007/s11664-017-5469-x.

39 K. Rambabu, G. Bharath, F. Banat and P. L. Show, Green synthesis of zinc oxide nanoparticles using *Phoenix dactylifera* waste as bioreductant for effective dye degradation and antibacterial performance in wastewater treatment, *J. Hazard. Mater.*, 2021, **402**, 123560, DOI: 10.1016/j.jhazmat.2020.123560.

40 M. Fang, C. M. Tang and Z. W. Liu, Microwave-assisted hydrothermal synthesis of Cu-doped ZnO single crystal nanoparticles with modified photoluminescence and confirmed ferromagnetism, *J. Electron. Mater.*, 2018, **47**, 1390–1396, DOI: 10.1007/s11664-017-5928-4.

41 S. Kumaresan, K. Vallalperuman and S. Sathishkumar, A Novel one-step synthesis of Ag-doped ZnO nanoparticles for high performance photo-catalytic applications, *J. Mater. Sci.: Mater. Electron.*, 2017, **28**, 5872–5879, DOI: 10.1007/s10854-016-6260-0.

42 M. Golmohammadi, M. Honarmand and S. Ghanbari, A green approach to synthesis of ZnO nanoparticles using jujube fruit extract and their application in photocatalytic degradation of organic dyes, *Spectrochim. Acta, Part A*, 2020, **229**, 117961, DOI: 10.1016/j.saa.2019.117961.

43 S. S. Momeni, M. Nasrollahzadeh and A. Rustaiyan, Green synthesis of the Cu/ZnO nanoparticles mediated by *Euphorbia prolifera* leaf extract and investigation of their catalytic activity, *J. Colloid Interface Sci.*, 2016, **472**, 173–179, DOI: 10.1016/j.jcis.2016.03.042.

44 S. Saravanan, M. Silambarasan and T. Soga, Structural, morphological and optical studies of Ag-doped ZnO nanoparticles synthesized by simple solution combustion method, *Jpn. J. Appl. Phys.*, 2014, **53**, 11RF01, DOI: 10.7567/JJAP.53.11RF01.

45 F. Lekoui, R. Amrani, S. Hassani, E. Garoudja, W. Filali, M. Ouchabane, N. Hendaoui and S. Oussalah, On the substrate heating effects on structural, mechanical and linear/non-linear optical properties of Ag–Mn co-doped ZnO thin films, *Opt. Mater.*, 2024, **150**, 115151, DOI: 10.1016/j.optmat.2024.115151.

46 R. Amari, A. Guellil, S. Terchi, B. Deghfel, A. Zoukel, D. Allali, E. Benrezgua, A. Boukhari and A. A. Mohamad, Coprecipitation synthesis of transition metal (Al, Mn, Cu, Ag) doped zinc oxide nanopowders: Characterization, photocatalytic test, and comparison study, *J. Australas. Ceram. Soc.*, 2024, **60**, 653–662, DOI: 10.1007/s41779-023-00969-6.

47 Y. Zhao, W. Ding, Y. Xiao and P. Yang, First-principles study on p-type transformation of ZnO doped by Ag element, *Phys. B*, 2023, **657**, 414810, DOI: 10.1016/j.physb.2023.414810.

48 N. S. George, S. A. Kadam, S. Sreehari, L. M. Jose, Y. R. Ma and A. Aravind, Inquest on photocatalytic and antibacterial traits of low composition Cu doped ZnO nanoparticles, *Chem. Phys. Lett.*, 2023, **815**, 140351, DOI: 10.1016/j.cplett.2023.140351.

49 V. P. Dinesh, P. Biji, M. Kumaravel, A. K. Tyagi and M. Kamaruddin, Synthesis and characterization of hybrid ZnO@ Ag core-shell nanospheres for gas sensor applications, *Mater. Sci. Forum*, 2012, **710**, 710–768, DOI: 10.4028/www.scientific.net/MSF.710.768.

50 K. Bloch, S. M. Mohammed, S. Karmakar, S. Shukla, A. Asok, K. Banerjee, R. Patil-Sawant, N. H. M. Kaus, S. Thongmee and S. Ghosh, Catalytic dye degradation by novel phytofabricated silver/zinc oxide composites, *Front. Chem.*, 2022, **10**, 1013077, DOI: 10.3389/fchem.2022.1013077.

51 A. E. Noua, D. Kaya, G. Sigircik, T. Tuken, F. Karadag and A. Ekicibil, Enhanced photocatalytic activity in AgCu-decorated ZnO nanoparticles under UV and sunlight, *J. Mater. Sci.: Mater. Electron.*, 2024, **35**, 1220, DOI: 10.1007/s10854-024-12919-4.

52 C. Vivek, B. Balraj and S. Thangavel, Structural, optical and electrical behavior of ZnO@ Ag core–shell nanocomposite synthesized via novel plasmon-green mediated approach, *J. Mater. Sci.: Mater. Electron.*, 2019, **30**, 11220–11230, DOI: 10.1007/s10854-019-01467-x.

53 S. Verma, B. Tirumala Rao, J. Jayabalan, S. K. Rai, D. M. Phase, A. K. Srivastava and R. Kaul, Studies on growth of Au cube-ZnO core-shell nanoparticles for photocatalytic degradation of methylene blue and methyl orange dyes in aqueous media and in presence of different scavengers, *J. Environ. Chem. Eng.*, 2019, **7**, 103209, DOI: 10.1016/j.jece.2019.103209.

54 R. Ebrahimi, K. Hossienzadeh, A. Maleki, R. Ghanbari, R. Rezaee, M. Safari, B. Shahmoradi, H. Daraei, A. Jafari, K. Yetilmezsoy and S. H. Puttaiah, Effects of doping zinc oxide nanoparticles with transition metals (Ag, Cu, Mn) on photocatalytic degradation of Direct Blue 15 dye under UV and visible light irradiation, *J. Environ. Health Sci. Eng.*, 2019, **17**, 479–492, DOI: 10.1007/s40201-019-00366-x.

55 C. Abinaya, M. Marikkannan, M. Manikandan, J. Mayandi, P. Suresh, V. Shanmugaiah, C. Shanmugaiah, C. Ekstrum and J. M. Pearce, Structural and optical characterization and efficacy of hydrothermal synthesized Cu and Ag doped zinc oxide nanoplate bactericides, *Mater. Chem. Phys.*, 2016, **184**, 172–182, DOI: 10.1016/j.matchemphys.2016.09.039.

56 J. Iqbal, N. Safdar, T. Jan, M. Ismail, S. S. Hussain, A. Mahmood, S. Shahzad and Q. Mansoor, Facile synthesis as well as structural, Raman, dielectric and antibacterial characteristics of Cu doped ZnO nanoparticles, *J. Mater. Sci. Technol.*, 2015, **31**, 300–304, DOI: 10.1016/j.jmst.2014.06.013.

57 Udayabhanu, G. Nagaraju, H. Nagabhushana, D. Suresh, C. Anupama, G. K. Raghu and S. C. Sharma, *Vitis labruska* skin extract assisted green synthesis of ZnO super structures for multifunctional applications, *Ceram. Int.*, 2017, **43**, 11656–11667, DOI: 10.1016/j.ceramint.2017.05.351.

58 S. Vikal, Y. K. Gautam, S. Meena, V. Parewa, A. Kumar, A. Kumar, S. Meena, S. Kumar and B. P. Singh, Surface functionalized silver-doped ZnO nanocatalyst: A sustainable cooperative catalytic, photocatalytic and antibacterial platform for waste treatment, *Nanoscale Adv.*, 2023, **5**, 805–819, DOI: 10.1039/D2NA00864E.